

1
2
3
4
5
6
7

8 Two forms of Opa1 cooperate to complete fusion of the mitochondrial inner-membrane
9

10
11
12

13 Yifan Ge ¹, Xiaojun Shi ^{2,#}, Sivakumar Boopathys ¹, Julie McDonald ¹,
14 Adam W. Smith ², and Luke H. Chao ^{1,*}

15
16
17
18
19
20

21 ¹ Dept. of Molecular Biology - Massachusetts General Hospital; Dept. of Genetics - Harvard
22 Medical School, Boston, MA U.S.A.

23

24 ² Dept. of Chemistry - University of Akron, Ohio U.S.A.

25

26 * Corresponding Author

27

28 [#] Present Address: Rammelkamp Center for Research and Department of Medicine, Departments
29 of Medicine, MetroHealth System; Department of Physiology and Biophysics, School of
30 Medicine, Case Western Reserve University, Ohio U.S.A.

31

32 **Abstract**
33
34 Mitochondrial membrane dynamics is a cellular rheostat that relates metabolic function and
35 organelle morphology. Using an *in vitro* reconstitution system, we describe a mechanism for
36 how mitochondrial inner-membrane fusion is regulated by the ratio of two forms of Opa1. We
37 found that the long-form of Opa1 (l-Opa1) is sufficient for membrane docking, hemifusion and
38 low levels of content release. However, stoichiometric levels of the processed, short form of
39 Opa1 (s-Opa1) work together with l-Opa1 to mediate efficient and fast membrane pore opening.
40 Additionally, we found that excess levels of s-Opa1 inhibit fusion activity, as seen under
41 conditions of altered proteostasis. These observations describe a mechanism for gating
42 membrane fusion.

43
44
45 **Introduction**
46
47 Mitochondrial membrane fission and fusion is essential for generating a dynamic mitochondrial
48 network and regenerative partitioning of damaged components via mitophagy (1). Membrane
49 rearrangement is essential for organelle function (2, 3) and contributes to diversity in
50 mitochondrial membrane shape that can reflect metabolic and physiological specialization (4-6).
51
52 Mitochondrial membrane fusion in metazoans is catalyzed by the mitofusins (Mfn1/2) and Opa1
53 (the outer and inner membrane fusogens, respectively), which are members of the dynamin
54 family of large GTPases (7, 8) (**Figure 1A**). An important series of *in vitro* studies with purified
55 mitochondria showed that outer- and inner membrane fusion can be functionally decoupled (9,
56 10). Outer membrane fusion requires the Mfn1/2, while inner-membrane fusion requires Opa1.
57 Loss of Opa1 function results in a fragmented mitochondrial network, loss of mitochondrial
58 DNA, and loss of respiratory function (11, 12). Opa1 is the most commonly mutated gene in
59 Dominant Optic Atrophy, a devastating pediatric condition resulting in degeneration of retinal
60 ganglion cells. Mutations in Opa1 account for over a third of the identified cases of this form of
61 childhood blindness (13).

62

63 Like dynamin, Opa1 comprises a GTPase domain, helical bundle signaling element (BSE), and
64 stalk region (with a membrane-interaction insertion) (**Figure 1B**) (14-16). A recent crystal
65 structure of the yeast orthologue of Opa1, Mgm1, revealed this membrane-interaction insertion is
66 a ‘paddle’, which contains a series of hydrophobic residues that can dip into one leaflet of a
67 membrane bilayer (17).

68

69 Opa1 is unique for a dynamin family GTPase, because it is processed to generate two forms. The
70 unprocessed, N-terminal transmembrane anchored, long form is called l-Opa1. The
71 proteolytically processed short form, which lacks the transmembrane anchor, is called s-Opa1
72 (18). Opa1 is processed by two proteases in a region N-terminal to the GTPase domain. Opa1
73 activity is stimulated by membrane depolarization (19). Yme1L activity is coupled to respiratory
74 state. Both forms of the protein (s-Opa1 and l-Opa1) can interact with cardiolipin, a negatively
75 charged lipid enriched in the mitochondrial inner membrane. Opa1 GTPase activity is stimulated
76 by association with cardiolipin (20).

77

78 Recent structural studies of Mgm1 focused on a short form, s-Mgm1 construct (16). This
79 analysis revealed a series of self-assembly interfaces in Mgm1’s stalk region. One set of
80 interactions mediates a crystallographic dimer, and a second set, observed in both the crystal and
81 cryo-electron tomographic (cryo-ET) reconstructions, bridge dimers in helical arrays on
82 membrane tubes with both positive and negative curvature. The s-Mgm1 membrane tubes that
83 formed with negative curvature are especially intriguing, because of Opa1’s recognized role in
84 cristae regulation, and the correspondence of the *in vitro* tube topology with cristae inner-
85 membrane invaginations (9, 21). These self-assembled states were not mediated by GTPase-
86 domain dimers.

87

88 Integrative biophysical and structural insights have revealed how dynamin nucleotide-state is
89 coupled to GTPase-domain dimerization, stalk-mediated self-assembly and membrane
90 rearrangement (17, 22-24). For Opa1, the opposite reaction (fusion) is also likely to result from
91 nucleotide-dependent conformational changes, coupled domain rearrangement, and self-
92 assembly necessary to overcome the kinetic barriers of membrane merger. Recent crystal
93 structure and electron cryo-tomography reconstructions reveal self-assembly interfaces, and

94 conformational changes that rearrange cristae membranes (16). The specific fusogenic nucleotide
95 hydrolysis-driven conformational changes remain to be distinguished.

96

97 Classic studies of Mgm1, the yeast orthologue of Opa1, show that both long and short forms are
98 required for inner-membrane fusion (25, 26). Studies by David Chan's group, using mammalian
99 cells, also showed that both long and short forms of Opa1 are required (27), and that knock-down
100 of the Opa1 processing protease Yme1L results in a more fragmented mitochondrial network
101 (18). Since Yme1L activity is tied to respiratory state, supplying cells with substrates for
102 oxidative phosphorylation shifts the mitochondrial network to a more tubular state. Importantly,
103 Chan and colleagues cleanly demonstrate, with an *in vitro* purified mitochondria system using
104 protease inhibitors and an engineered cleavage site that mitochondrial fusion is dependent on
105 proteolytic processing (18). In contrast, work from the Langer group showed l-Opa1 alone was
106 sufficient for fusion when expressed in a YME1L *-/-*, OMA1 *-/-* background (6), indicating that
107 Opa1 processing is dispensable for fusion. Over-expression of s-Opa1 in this background
108 resulted in mitochondrial fragmentation, which was interpreted as a result of s-Opa1 mediated
109 fission. Is proteolytic processing of Opa1 required for regulating fusion? Is s-Opa1 required for
110 fusion?

111

112 In this study, we applied a TIRF-based supported bilayer/liposome assay (**Figure 1C**), to
113 distinguish the sequential steps in membrane fusion that convert two apposed membranes into
114 one continuous bilayer: tethering, membrane docking, lipid mixing (hemifusion) and content
115 release (**Figure 1D**). This format allows control of protein levels for all components introduced
116 into the system. Previous *in vitro* reconstitution studies from Ishihara and colleagues (28) were
117 performed in bulk. The analysis we present here resolves individual fusion events in the TIRF
118 field and is more sensitive than bulk measurements. In addition, our assay records kinetic data
119 lost in ensemble averaging. Finally, the assay as applied here, can distinguish stages of fusion for
120 individual liposomes. Tethering is observed when liposomes attach to the supported bilayer.
121 Lipid mixing (hemifusion) is reported when a liposome dye (TexasRed) diffuses into the
122 supported bilayer. Release of a soluble content dye (calcein) from within the liposome (loaded at
123 quenched concentrations) indicates full pore opening. Our assay includes a content reporter dye

124 in all conditions, so we can relate each intermediate with full fusion, for example, comparing
125 instances where there may be lipid mixing, but no content release.

126

127 Using this *in vitro* reconstitution approach, we describe key mechanistic requirements for
128 mitochondrial inner-membrane fusion. We report efficiency and kinetics for each step in Opa1-
129 mediated fusion. These experiments describe the membrane activities of l-Opa1 alone, s-Opa1
130 alone, and l-Opa1:s-Opa1 together. We find that s-Opa1 and l-Opa1 are both required for
131 efficient and fast pore opening, and present a mechanism for how the ratio of l-Opa1 and s-Opa1
132 levels regulate inner-membrane fusion. These results are compatible and expand the original
133 yeast observations (25), explain previous cellular studies (6, 18), and contextualizes recent *in*
134 *vitro* observations (28). The data presented here unambiguously describe the activities of Opa1,
135 contributing to a more complete model for how inner-membrane fusion is regulated.

136

137 **Results**

138

139 **Assay validation**

140 We purified long and short forms of human Opa1 expressed in *Pichia pastoris*. Briefly, Opa1
141 was extracted from membranes using n-dodecyl-β-D-maltopyranoside (DDM) and purified by
142 Ni-NTA and Strep-tactin affinity chromatography, and size exclusion chromatography (**Figure**
143 **2A**). A series of short isoforms are observed *in vivo* (11, 29). In this study, we focused on a short
144 form corresponding to the S1 isoform resulting from Oma1 cleavage (**Figure 2B**). GTPase
145 activity of purified Opa1 was confirmed by monitoring free phosphate release (**Figure 2C & D**).
146 Opa1 activity was enhanced by the presence of cardiolipin, consistent with previous reports
147 (**Figure 2C & D, Figure 2-figure supplement 1**) (20).

148

149 We reconstituted l-Opa1 into 200 nm liposomes and supported bilayers generated by Langmuir-
150 Blodgett/Langmuir-Schaefer methods (30). l-Opa1 was added to liposomes and a supported
151 bilayer at an estimated protein:lipid molar ratio of 1:5000 and 1:50000, respectively. Membranes
152 comprised DOPE (20%), Cardiolipin (20%), PI (7%), and DOPC (52.8%). Reporter dyes (e.g.
153 Cy5-PE, TexasRed-PE) were introduced into the supported bilayer and liposome membranes,
154 respectively, at ~0.2 % (mol). A surfactant mixture stabilized the protein sample during

155 incorporation. Excess detergent was removed using Bio-Beads and dialysis. We confirmed
156 successful reconstitution by testing the stability of l-Opa1 incorporation under high salt and
157 sodium carbonate conditions, and contrasting these results with s-Opa1 peripheral membrane
158 association (**Figure 2-figure supplement 2**).

159

160 We evaluated reconstitution of l-Opa1 into both the polymer-tethered supported lipid bilayers
161 and proteoliposomes using two approaches. First, using Fluorescence Correlation Spectroscopy
162 (FCS), we measured the diffusion of dye-conjugated lipids and antibody-labeled protein. FCS
163 intensity measurements confirmed ~75% of l-Opa1 reconstituted into the bilayer in the
164 accessible orientation. Bilayer lipid diffusion was measured as $1.46 \pm 0.12 \mu\text{m}^2/\text{s}$, while the
165 diffusion coefficient of bilayer-reconstituted l-Opa1 was $0.88 \pm 0.10 \mu\text{m}^2/\text{s}$ (**Figure 2-figure**
166 **supplement 3**), which is in agreement with previous reports of lipid and reconstituted
167 transmembrane protein diffusion (31). These measurements indicate the reconstituted l-Opa1 in
168 the bilayer can freely diffuse, and has the potential to self-associate and oligomerize. Blue native
169 polyacrylamide gel electrophoresis (BN-PAGE) analysis also show the potential for the purified
170 material to self-assemble (**Figure 2-figure supplement 4**). FCS experiments were also
171 performed on liposomes. FCS intensity measurements confirmed 86.7% of total introduced l-
172 Opa1 successfully reconstituted into the liposomes. The diffusion coefficient of free antibody
173 was $163.87 \pm 22.27 \mu\text{m}^2/\text{s}$. The diffusion coefficient for liposomes labeled with a lipid dye was
174 $2.22 \pm 0.33 \mu\text{m}^2/\text{s}$, and the diffusion coefficient for l-Opa1 proteoliposomes bound to a TexasRed
175 labeled anti-His antibody was $2.12 \pm 0.36 \mu\text{m}^2/\text{s}$ (**Figure 2-figure supplement 5**). Second, we
176 measured the number of l-Opa1 incorporated into liposomes by fluorescent step-bleaching of
177 single proteoliposomes (**Figure 2E & F**). We found an average step number of 2.7 for individual
178 l-Opa1-containing proteoliposomes labeled with TexasRed conjugated anti-His antibody, when
179 tethered to cardiolipin containing lipid bilayers (**Figure 2G**).

180

181 **Nucleotide-dependent bilayer tethering and docking**

182 Using the supported bilayer/liposome assay sketched in **Figure 1C**, we found that l-Opa1 tethers
183 liposomes in a homotypic fashion (**Figure 3A**), as reported by the appearance of TexasRed
184 puncta in the TIRF field above a l-Opa1-containing bilayer. This interaction occurred in the
185 absence of nucleotide (apo, nucleotide-free) but was enhanced by GTP. We next investigated

186 requirements for Opa1 tethering. In the absence of cardiolipin, addition of GTP did not change
187 the number of tethered particles under otherwise identical conditions (**Figure 3B**). In contrast,
188 with cardiolipin-containing liposomes and bilayers, homotypic l-Opa1:l-Opa1 tethering is
189 enhanced by GTP. Non-hydrolyzable analogues (GMPPCP) disrupt tethering (**Figure 3C**), and a
190 hydrolysis-dead mutant (G300E) l-Opa1 shows little tethering (**Figure 3-figure supplement**
191 **1B**), supporting a role for the hydrolysis transition-state in tethering, as observed for atlastin (32,
192 33). Bulk light scattering measurements of liposome size distributions (by NTA Nanosight) show
193 l-Opa1-mediated liposome clustering requires the presence of GTP (**Figure 3-figure**
194 **supplement 2**). These bulk measurements show a GTP-dependent increase in observed particle
195 size.

196

197 Ban, Ishihara and colleagues have observed a heterotypic, fusogenic interaction between l-Opa1
198 on one bilayer and cardiolipin in the opposing bilayer (28). Inspired by this work and our own
199 observations, we considered if a heterotypic interaction between l-Opa1 and cardiolipin on the
200 opposing membrane could contribute to l-Opa1-mediated tethering (**Figure 3D**). Indeed, we find
201 that proteoliposomes containing l-Opa1 will tether to a cardiolipin-containing bilayer lacking any
202 protein binding partner, presumably mediated by the lipid-binding ‘paddle’ insertion in the
203 helical stalk region (16). This tethering is cardiolipin-dependent, as l-Opa1 containing bilayers
204 do not tether DOPC liposomes (**Figure 4-figure supplement 1B**).

205

206 We next measured whether s-Opa1, lacking the transmembrane anchor, could tether membranes
207 via membrane binding interactions that bridge the two bilayers. We observe that s-Opa1 (added
208 at a protein:lipid molar ratio of 1:5000) can tether cardiolipin liposomes to a cardiolipin-
209 containing planar bilayer, as observed previously for Mgm1 (34). Further, this s-Opa1 tethering
210 is enhanced by the presence of GTP (**Figure 3E**). Previous reports observed membrane
211 tubulation at higher concentrations of s-Opa1 (0.2 mg/ml, 1.67 nmol) (20). Under the lower s-
212 Opa1 concentrations in our experiments (0.16 µg/ml, 2×10⁻³ nmol), the supported bilayer
213 remains intact (before and after GTP addition), and we do not observe any evidence of tubular
214 structures forming in the liposomes or bilayers.

215

216 Our experiments indicate that s-Opa1 alone can induce tethering. Is s-Opa1 competent for close
217 docking of membranes? To answer this, we evaluated close bilayer approach using a reporter for
218 when membranes are brought within FRET distances (~40-60 Å). This FRET signal reports on
219 close membrane docking when a TexasRed conjugated PE is within FRET distance of a Cy5-
220 conjugated PE. We observed a low FRET signal for tethered membranes, when the FRET pair is
221 between two supported bilayers tethered via PEG spacer (average distance between the bilayer
222 centers of ~7 nm), compared to a single bilayer containing both of the FRET pair (**Figure 4-**
223 **figure supplement 1A**). When l-Opa1 is present on both bilayers (homotypic arrangement), or
224 on only one bilayer (heterotypic arrangement), efficient docking occurs in the presence of
225 cardiolipin, as reported by a FRET signal with efficiencies of ~40% (**Figure 4B & C and Figure**
226 **4-figure supplement 1A**). Efficient homotypic docking requires GTP hydrolysis. GMPPCP
227 prevents homotypic docking of l-Opa1, and abolishes the heterotypic l-Opa1 signal) (**Figure**
228 **4A**). In contrast, s-Opa1 alone does not bring the two bilayers within FRET distance, consistent
229 with observations for s-Mgm1 tethered bilayers (**Figure 4A**) (34). The distances between two
230 paddles in the s-Mgm1 dimer is ~120 Å. Tethering mediated by two paddle interactions would
231 be compatible with our observed low FRET signal when s-Opa1 engages two bilayers (17).

232

233 **Hemifusion and pore opening**

234 We find that l-Opa1, when present on only one bilayer, in a heterotypic format, can mediate
235 close membrane docking (**Figure 4A**). To quantify hemifusion (lipid exchange), we measured
236 the fluorescence intensity decay times for the liposome dye (TexasRed) as it diffuses into the
237 bilayer during lipid mixing. Analysis of particle dye diffusion kinetics show that in this
238 heterotypic format, l-Opa1 can induce hemifusion (**Figure 5A**). The hemifusion efficiency
239 (percentage of total particles where the proteoliposome dye diffuses into the supported bilayer)
240 for heterotypic l-Opa1 was <5% (**Figure 6A**). Previously published *in vitro* bulk liposome-based
241 observations for heterotypic l-Opa1 lipid mixing observed hemifusion efficiencies of 5-10%,
242 despite higher protein copy number per liposome (28). We next compared homotypic l-Opa1
243 catalyzed hemifusion and observed shorter mean dwell times than heterotypic l-Opa1 (**Figure 5B**
244 & **5C, Figure 5-figure supplement 1**). In our assay, we observe homotypic l-Opa1 induces
245 hemifusion more efficiently than heterotypic l-Opa1. We measured a homotypic l-Opa1
246 hemifusion efficiency of ~15% (**Figure 6A**). For comparison, *in vitro* measurements of viral

247 membrane hemifusion, show efficiencies of ~25-80% (35, 36). This comparison is imperfect, as
248 viral particles have many more copies of their fusion proteins on their membrane surface and
249 viral fusogens do not undergo multiple cycles of nucleotide hydrolysis, like Opa1.

250

251 Following hemifusion, pore opening is the key step where both leaflets merge and content from
252 the two compartments can mix. We observed pore opening by monitoring content dye (calcein)
253 release under these conditions (37). Of all homotypic tethered particles, ~18% undergo
254 hemifusion. Of these particles undergoing hemifusion, approximately half proceed to full fusion
255 (8% of all homotypic tethered particles). Both s-Opa1 alone (at 0.16 µg/ml, or 2×10^{-3} nmol
256 concentration), or l-Opa1 in the heterotypic format did not release content (**Figure 6A**). In
257 contrast, ~8% of homotypic l-Opa1:l-Opa1 particles undergo pore opening and content release.
258 These observations indicate, l-Opa1 alone is sufficient for pore opening, while s-Opa1 alone or
259 heterotypic l-Opa1 are insufficient for full fusion.

260

261 **Ratio of s-Opa1:l-Opa1 regulate pore opening efficiency and kinetics**

262 Our observation that l-Opa1 is sufficient for pore opening leaves open the role of s-Opa1 for
263 fusion. Previous studies suggest an active role for s-Mgm1 (the yeast orthologue of s-Opa1) in
264 fusion (25). In this work, l-Mgm1 GTPase activity was dispensable for fusion in the presence of
265 wild-type s-Mgm1 (25). Work in mammalian cells suggest different roles for s-Opa1. Studies
266 from the Chan group showed Opa1 processing helps promote a tubular mitochondrial network
267 (18). In contrast, other studies showed upregulated Opa1 processing in damaged or unhealthy
268 mitochondria, resulting in accumulation of s-Opa1 and fragmented mitochondria (18, 28, 38).
269 The interpretation of the latter experiments was that, in contrast to the yeast observations, s-Opa1
270 suppresses fusion activity. Furthermore, studies using Opa1 mutations that abolish processing of
271 l-Opa1 to s-Opa1 suggest the short form is dispensable for fusion, and s-Opa1 may even mediate
272 fission (39, 40). These different, and at times opposing, interpretations of experimental
273 observations have been difficult to reconcile.

274

275 To address how s-Opa1 and l-Opa1 cooperate, we added s-Opa1 to the l-Opa1 homotypic
276 supported bilayer/liposome fusion experiment. l-Opa1-only homotypic fusion has an average
277 dwell time of 20 s and an efficiency of ~10% (**Figure 6B-E & Figure 6-figure supplement 1**).

Upon addition of s-Opa1, we observe a marked increase in pore opening efficiency, reaching 80% at equimolar l-Opa1 and s-Opa1 (**Figure 6B**). At equimolar levels of s-Opa1, we also observe a marked change in pore opening kinetics, with a four-fold decrease in mean dwell time (**Figure 6C**). The efficiency peaks at an equimolar ratio of s-Opa1 to l-Opa1, showing that s-Opa1 cooperates with l-Opa1 to catalyze fast and efficient fusion. When s-Opa1 levels exceed l-Opa1 (at a 2:1 ratio or greater), particles begin to detach, effectively reducing fusion efficiency. This is consistent with a dominant negative effect, where s-Opa1 likely disrupts the homotypic l-Opa1:l-Opa1 interaction. We quantified particle untethering, and observe a dose-dependent detachment of l-Opa1:l-Opa1 tethered particles with the addition of G300E s-Opa1 (**Figure 3-figure supplement 1A**).

288

289 Discussion

290

Our experiments suggest different assembled forms of Opa1 represent functional intermediates along the membrane fusion reaction coordinate, each of which can be a checkpoint for membrane fusion and remodeling. We show that s-Opa1 alone is sufficient to mediate membrane tethering but is unable to dock and merge lipids in the two bilayers, and thus, insufficient for hemifusion (**Figure 7A**). In contrast, l-Opa1, in a heterotypic format, can tether and hemifuse bilayers, but is unable to transition through the final step of pore opening (**Figure 7B**). Homotypic l-Opa1 can hemifuse membranes and mediate low levels of pore opening (**Figure 7C i.**). However, our results show that s-Opa1 and l-Opa1 together, synergistically catalyze efficient and fast membrane pore opening (**Figure 7C ii.**). Importantly, we find that excess levels of s-Opa1 are inhibitory for pore opening, providing a means to down-regulate fusion activity (**Figure 7C iii.**).

302

Our model proposes that l-Opa1:s-Opa1 stoichiometry gates the final step of fusion, pore opening. Electron tomography studies of mitofusin show a unevenly distributed ring of proteins clustering at an extensive site of close membrane docking, but only local regions of pore formation (41). Our study is consistent with local regions of contact and low protein copy number mediating lipid mixing and pore formation (42). Our study would predict that s-Opa1 enrichment in regions of the mitochondrial inner-membrane would suppress fusion. This study

309 did not explore the roles of s-Opa1 assemblies (helical or 2-dimensional) in fusion (16). Cellular
310 validation of our proposed model, and other states, will require correlating l-Opa1:s-Opa1 ratio
311 and protein spatial distribution with fusion efficiency and kinetics. This studied focused on the
312 S1 form of s-Opa1. The behavior of other Opa1 splice isoforms, which vary in the processing
313 region, remains another important area for future investigation (43).

314

315 The results and model presented here help resolve the apparent contradicting nature of the Chan
316 and Langer cellular observations. As observed by the Langer group, l-Opa1 alone in our system,
317 is indeed sufficient for full fusion, albeit at very low levels (6). The activity of unprocessed Opa1
318 was not ruled out in previous studies of Chan and colleagues (18). In contrast to the Langer
319 group's conclusions, we find that s-Opa1 strongly stimulates l-Opa1-dependent fusion activity,
320 independent of the Yme1L processing reaction (18). Under conditions of s-Opa1 overexpression,
321 Langer *et al.* observed, a fragmented mitochondrial network. We do not see any evidence for
322 fission or fusion, for s-Opa1 alone, under our reconstitution conditions. Instead, our data and
323 model suggest this is due to s-Opa1 disrupting l-Opa1 activity, swinging the membrane dynamics
324 equilibrium toward fission.

325

326 Mitochondrial dysfunction is often associated with Opa1 processing (44). The activity of the
327 mitochondrial inner-membrane proteases, Yme1L and Oma1, is regulated by mitochondrial
328 matrix state, thereby coupling organelle health to fusion activity (6, 40, 44-46). Basal levels of
329 Opa1 cleavage are observed in healthy cells (18). Upon respiratory chain collapse and membrane
330 depolarization increased protease activity elevates s-Opa1 levels, downregulating fusion (47).
331 Our results point to the importance of basal Opa1 processing, and are consistent with
332 observations that both over-processing and under-processing of l-Opa1 can result in a loss of
333 function (6).

334

335 Key questions remain in understanding the function of different Opa1 conformational states, and
336 the nature of a fusogenic Opa1 complex. Recent structural studies show s-Mgm1 self-assembles
337 via interfaces in the stalk region (16, 48). The nucleotide-independent tethering we observe also
338 implicate stalk region interactions, outside of a GTPase-domain dimer, in membrane tethering.
339 How does nucleotide hydrolysis influence these interactions during fusion? Outstanding

340 questions also remain in understanding the cooperative interplay between local membrane
341 environment, s-Opa1, and l-Opa1. Could the cooperative activity of l-Opa1 and s-Opa1 be
342 mediated by direct protein-protein interactions, local membrane change, or both? Could tethered
343 states (e.g. homotypic l-Opa1 or heterotypic l-Opa1) bridge bilayers to support membrane
344 spacings seen in cristae? Answers to these questions, and others, await further mechanistic
345 dissection to relate protein conformational state, *in situ* architecture and physiological regulation.

346

347

348 **Acknowledgements**

349

350 We thank members of the Chao lab for helpful discussions and review of the manuscript. LHC is
351 grateful for support from a Charles H. Hood Foundation Child Health Research Award. We
352 thank Fanny Ng and the Szostak Lab for technical support. Work by XS and AWS are supported
353 by the National Science Foundation under Grant No. CHE-1753060.

354

355 **Competing interests**

356

357 None

358 Materials and Methods

359

Key Resources Table				
Reagent type (species) or resource	Designati on	Source or reference	Identifiers	Additional information
Chemical compound, drug	18:1 (Δ 9-Cis) PC (DOPC)	Avanti Polar lipids	Cat #: 850375P	
Chemical compound, drug	1',3'-bis[1,2-dioleoyl-sn-glycero-3-phospho]-glycerol (sodium salt)	Avanti Polar lipids	Cat #: 710335P	
Chemical compound, drug	1,2-dioleoyl-sn-glycero-3-phosphoethanolamine-N-[methoxy(polyethylene glycol)-2000] (ammonium salt)	Avanti Polar lipids	Cat #: 880130P	
Chemical compound, drug	L- α -lysophosphatidylinositol (Liver, Bovine) (sodium salt)	Avanti Polar lipids	Cat #: 850091P	

Chemical compound, drug	1-palmitoyl-2-oleoyl-sn-glycero-3-phosphoethanolamine	Avanti Polar lipids	Cat #: 850757P	
Chemical compound, drug	Texas Red™ 1,2-Dihexadecanoyl-sn-Glycero-3-Phosphoethanolamine, Triethylammonium Salt (Texas Red™ DHPE)	ThermoFisher Scientific	Cat #: T1395MP	
Chemical compound, drug	1,2-dioleoyl-sn-glycero-3-phosphoethanolamine-N-(Cyanine 5)	Avanti polar lipid	Cat #: 810335C1mg	
Chemical compound, drug	Calcein	Sigma-Aldrich	Cat #: C0875; PubChem Substance ID: 24892279	
strain	<i>Pichia pastoris</i> SMD1163 (<i>his4, pep, prb1</i>)	Rapoport lab; Harvard Medical School.		
Recombinant DNA reagent	pPICZ A-TwinStrep-IOPA1-H ₁₀	GenScript		plasmid to transform and express human WT I-Opa1 (isoform1).
Recombinant DNA reagent	pPICZ A-TwinStrep-sOPA1-H ₁₀	GenScript		plasmid to transform and express human WT s-Opa1 (s1).

Recombinant DNA reagent	pPICZ A-TwinStrep-IOPA1 (G300E)-H ₁₀	GenScript		plasmid to transform and express G300E mutant of I-Opa1 (isoform 1).
Recombinant DNA reagent	pPICZ A-TwinStrep-sOPA1 (G300E)-H ₁₀	GenScript		plasmid to transform and express G300E mutant of s-Opa1 (s1).
Antibody	Rabbit Anti-Opa1 antibody	NOVUS BIOLOGICALS	Cat #: NBP2-59770	Western Blot 2 ug/ml
Antibody	Mouse 6x-His Tag Monoclonal Antibody (HIS.H8)	ThermoFisher Scientific	Cat #: MA1-21315	Western Blot 1:2000
Antibody	Mouse StrepMAB-Classic, HRP conjugate (2-1509-001)	IBA Lifesciences	Cat #: 2-1509-001	Western Blot 1:2500/1:32000
Antibody	Rabbit IgG HRP Linked Whole Ab	SIGMA-ALDRICH INC	Cat #: GENA934-1ML	
Antibody	Mouse IgG HRP Linked Whole Ab	SIGMA-ALDRICH INC	Cat #: GENA931-1ML	
Chemical compound, drug	GTP Disodium salt	SIGMA-ALDRICH INC	Cat #: 10106399001	
Commercial assay, kit	EnzChek™ Phosphate Assay Kit	ThermoFisher Scientific	Cat #: E6646	
Chemical compound, drug	GppCp (Gmppcp), Guanosine-5'-[β , γ -methyleno]tr	Jena Bioscience	Cat #: NU-402-5	

	iphosphate, Sodium salt			
Chemical compound, drug	n-Dodecyl- β-D-Maltopyranoside	Anatrace	Cat #: D310 25 GM	
Chemical compound, drug	n-Octyl-α-D-Glucopyranoside	Anatrace	Cat #: O311HA 25 GM	
Chemical compound, drug	Lauryl Maltose Neopentyl Glycol (LMNG)	Anatrace	Cat #: NG310	
Chemical compound, drug	LMNG-CHS Pre-made solution	Anatrace	Cat #: NG310-CH210	
Chemical compound, drug	Zeocin	Invivogen	Cat #: ant-zn-1p	
Chemical compound, drug	Ni-NTA	Biorad	Cat #: 7800812	
Chemical compound, drug	StrepTactin XT	IBA Lifesciences	Cat #: 2-4026-001	
Chemical compound, drug	Biotin	IBA Lifesciences	Cat #: 2-1016-005	
Chemical compound, drug	Superose 6 Increase 10/300 GL	GE	Cat #: 29091596	
Chemical compound, drug	TEV protease	Prepared in lab, purchased from GenScript	Cat #: Z03030	
Chemical compound, drug	Benzonase Nuclease	Sigma-Aldrich	Cat #: E1014	

Chemical compound, drug	Protease inhibitor cocktail	Roche	Cat #: 05056489001	
Chemical compound, drug	Leupeptin	Sigma-Aldrich	Cat #: L2884	
Chemical compound, drug	Pepstatin A	Sigma-Aldrich	Cat #: P5318	
Chemical compound, drug	Benzamidine hydrochloride hydrate	Sigma-Aldrich	Cat #: B6506	
Chemical compound, drug	Phenylmethylsulfonyl fluoride (PMSF)	Sigma-Aldrich	Cat #: 10837091001	
Chemical compound, drug	Aprotinin	Sigma-Aldrich	Cat #: A1153	
Chemical compound, drug	Trypsin inhibitor	Sigma-Aldrich	Cat #: T9128	
Chemical compound, drug	Bestatin	GoldBio	Cat #: B-915-100	
Chemical compound, drug	E-64	GoldBio	Cat #: E-064-25	
Chemical compound, drug	Phosphoramidon disodium salt	Sigma-Aldrich	Cat #: R7385	
Commercial assay, kit	3-12% Bis-Tris Protein Gels	ThermoFisher Scientific	BN1003BOX	
Commercial assay, kit	NativePAGE Running Buffer Kit	ThermoFisher Scientific	BN2007	

Commercial assay, kit	NativePAGE 5% G-250 Sample Additive	ThermoFisher Scientific	BN2004	
Commercial assay, kit	NativePAGE Sample Buffer (4X)	ThermoFisher Scientific	BN2003	
software, algorithm	Slidebook	Intelligent imaging	RRID: SCR_014300	
software, algorithm	Fiji /ImageJ	Fiji	SCR_002285	
software, algorithm	FCS analysis tool	Smith Lab, University of Akron		

360

361

362 **Expression and purification**

363 Genes encoding l- (residues 88-960) or s- (residues 195-960) OPA1 (UniProt O60313-1) were
 364 codon optimized for expression in *Pichia pastoris* and synthesized by GenScript (NJ, USA). The
 365 sequences encode Twin-Strep-tag, HRV 3C site, (G₄S)₃ linker at the N-terminus and (G₄S)₃
 366 linker, TEV site, deca-histidine tag at the C-terminus. The plasmids were transformed into the
 367 methanol inducible SMD1163 strain (gift from Dr. Tom Rapoport, Harvard Medical School) and
 368 the clones exhibiting high Opa1 expression were determined using established protocols. For
 369 purification, cells expressing l-Opa1 were resuspended in buffer A (50 mM sodium phosphate,
 370 300 mM NaCl, 1 mM 2-mercaptoethanol, pH 7.5) supplemented with benzonase nuclease and
 371 protease inhibitors and lysed using an Avestin EmulsiFlex-C50 high-pressure homogenizer. The
 372 membrane fractions were collected by ultracentrifugation at 235,000 x g for 45 min. at 4 °C. The
 373 pellet was resuspended in buffer A containing 2% DDM, (Anatrace, OH, USA) 0.1 mg/ml 18:1
 374 cardiolipin (Avanti Polar Lipids, AL, USA) and protease inhibitors and stirred at 4 °C for 1 hr.
 375 The suspension was subjected to ultracentrifugation at 100,000 x g for 1 hr at 4 °C. The extract
 376 containing l-Opa1 was loaded onto a Ni-NTA column (Biorad, CA, USA), washed with 40
 377 column volumes of buffer B (50 mM sodium phosphate, 350 mM NaCl, 1 mM 2-
 378 mercaptoethanol, 1 mM DDM, 0.025 mg/ml 18:1 cardiolipin, pH 7.5) containing 25 mM

379 imidazole and 60 column volumes of buffer B containing 100 mM imidazole. The bound protein
380 was eluted with buffer B containing 500 mM imidazole, buffer exchanged into buffer C (100
381 mM Tris-HCl, 150 mM NaCl, 1 mM EDTA, 1 mM 2-mercaptoethanol, 0.15 mM DDM, 0.025
382 mg/ml 18:1 cardiolipin, pH 8.0). In all the functional assays, the C-terminal His tag was cleaved
383 by treatment with TEV protease and passed over the Ni-NTA and Strep-Tactin XT Superflow
384 (IBA Life Sciences, Göttingen, Germany) columns attached in tandem. The Strep-Tactin XT
385 column was detached, washed with buffer C and eluted with buffer C containing 50 mM biotin.
386 The elution fractions were concentrated and subjected to size exclusion chromatography in
387 buffer D (25 mM BIS-TRIS propane, 100 mM NaCl, 1 mM TCEP, 0.025 mg/ml 18:1
388 cardiolipin, pH 7.5, 0.01% LMNG, 0.001% CHS). s-OPA1 was purified using a similar approach
389 but with one difference: post lysis, the DDM was added to the unclarified lysate at 0.5%
390 concentration and stirred for 30 min. – 1 hr. at 4 °C prior to ultracentrifugation. The supernatant
391 was applied directly to the Ni-NTA column.

392

393 **GTPase activity assay**

394 The GTPase activity of purified Opa1 was analyzed using EnzCheck Phosphate Assay Kit
395 (Thermo Fisher, USA) according to the vendor's protocol. Each condition was performed in
396 triplicate. The GTPase assay buffers contained 25 mM HEPES, 60 mM NaCl, 100 mM KCl, 0.5
397 mM MgCl₂ with 0.15 mM DDM. 60 µM GTP was added immediately before data collection. To
398 compare the effect of cardiolipin on GTPase activity, additional 0.5 mg/ml Cardiolipin was
399 dissolved in the reaction buffer and added to the reaction to a final concentration of 0.02 mg/ml.
400 The absorbance at 340 nm of each reaction mixture was recorded using SpectraMax i3 plate
401 reader (Molecular Devices) every 30 seconds. Experiments were performed in triplicate.
402 Resulting Pi concentration was fitted to a single-phase exponential-decay, specific activity data
403 were fitted to a Michaelis-Menten equation (GraphPad Prism 8.1).

404

405 **Preparation of polymer-tethered lipid bilayers**

406 Lipid reagents, including 1,2-dioleoyl-sn-glycero-3-phosphocholine, (DOPC); 1,2-dioleoyl-sn-
407 glycero-3-phosphoethanolamine-N-[methoxy(polyethylene glycol)-2000] (DOPE-PEG2000), L-
408 α-phosphatidylinositol (Liver PI) and 1',3'-bis[1,2-dioleoyl-sn-glycero-3-phospho]-glycerol
409 (cardiolipin) were purchased from Avanti Polar Lipids (AL, USA). To fabricate the polymer-

410 tethered lipid bilayers, we combined Langmuir-Blodgett and Langmuir-Schaefer techniques,
411 using a Langmuir-Blodgett Trough (KSV-NIMA, NY, USA) (31, 49). For cardiolipin-free lipid
412 bilayers, a lipid mixture with DOPC with 5 % (mol) DOPE-PEG2000 and 0.2 % (mol) Cy5-
413 DSPE at the total concentration of 1 mg/ml was spread on the air water interface in a Langmuir
414 trough. The surface pressure was kept at 30 mN/m for 30 minutes before dipping. The first lipid
415 monolayer was transferred to the glass substrate (25 mm diameter glass cover slide, Fisher
416 Scientific, USA) through Langmuir-Blodgett dipping, where the dipper was moved up at a speed
417 of 22.5 mm/min. The second leaflet of the bilayer was assembled through Langmuir-Schaefer
418 transfer after 1 mg/ml of DOPC with 0.2 % (mol) Cy5-PE (Avanti Polar Lipids, AL, USA) was
419 applied to an air-water interface and kept at a surface pressure of 30 mN/m.

420

421 Lipid bilayer with cardiolipin was fabricated in a similar manner, where the bottom leaflet
422 included 7 % (mol) Liver PI, 20 % (mol) cardiolipin, 20 % (mol) DOPE, 5 % (mol) DOPE-
423 PEG2000, 0.2 % (mol) Cy5-PE and 47.8% DOPC. The composition of the top leaflet of the
424 bilayer was identical except for the absence of DOPE-PEG2000. To match the area/molecule at
425 the air-water interface between CL-free and CL-containing bilayer, the film pressure was kept at
426 37 mN/m. The final average area per lipid, which is the key factor affecting lipid lateral mobility,
427 was kept constant at a $A_{\text{lipid}} = 65 \text{ \AA}^2$ (50).

428

429 Double bilayers were fabricated according to previous reports (51). The first bilayer containing
430 DOPC with 5 % (mol) DSPE-PEG2000-Maleimide (Avanti Polar Lipids, AL, USA) and 0.2 %
431 (mol) Cy5-DOPE in both inner and outer leaflets was made using Langmuir-Blodgett/Langmuir-
432 Schaefer methods. The second planar lipid bilayer was formed by fusion of lipid vesicles and
433 removal of non-fused vesicles. Lipid vesicles were formed by hydrating dried lipid films with
434 DOPC, 0.2 % (mol) TexasRed-DHPE and 5 % (mol) of linker lipid (DPTE, AL, USA) in a 0.1
435 mM sucrose/1 mM CaCl₂ solution. The lipid suspension was heated for 1.5 hours at 75 °C, and
436 added to the first bilayer in a 0.1 mM glucose/1 mM CaCl₂ solution. After 2 hours of incubation,
437 additional vesicles were removed by extensive rinsing. The bilayer was then imaged by TIRF
438 microscope.

439

440 **Reconstitution of l-Opa1 into lipid bilayers**

441 Purified l-Opa1 was first desalted into 25 mM Bis-Tris buffer with 150mM NaCl containing 1.2
442 nM DDM and 0.4 µg/L of cardiolipin to remove extra surfactant during purification. The
443 resulting protein was added to each bilayer to the total amount of 1.3×10^{-12} mol (protein:lipid
444 1:10000) together with a surfactant mixture of 1.2 nM of DDM and 1.1 nM n-Octyl- β -D-
445 Glucopyranoside (OG, Anatrace, OH, USA). The protein was incubated for 2 hours before
446 removal of the surfactant. To remove the surfactant, Bio-Beads SM2 (Bio-Rad, CA, USA) was
447 added to the solution at a final concentration of 10 µg beads per mL of solution and incubated for
448 10 minutes. Buffer with 25 mM Bis-Tris and 150 mM NaCl was applied to remove the Bio-
449 beads with extensive washing. Successful reconstitution was determined using fluorescent
450 correlation spectroscopy assay as described in the supplemental materials.

451

452 **Preparation of liposomes and proteoliposomes**

453 To prepare calcein (MilliporeSigma, MA, USA) encapsulated liposomes, lipid mixtures (7 %
454 (mol) PI, 20% cardiolipin, 20% PE, 0.2% TexasRed-PE, DOPC (52.8%)), were dissolved in
455 chloroform and dried under argon flow for 25 minutes. The resulting lipid membrane was mixed
456 in 25 mM Bis-Tris with 150mM NaCl and 50 mM calcein through vigorous vortexing. Lipid
457 membranes were further hydrated by incubating the mixtures under 70 °C for 30 min. Large
458 unilamellar vesicles (LUVs) were prepared by extrusion (15 to 20 times) using a mini-extruder
459 with 200 nm polycarbonate membrane.

460

461 Proteoliposomes were prepared by adding purified l-Opa1 in 0.1 µM DDM to prepared
462 liposomes at a protein: lipid of 1:5000 (2.5 µg l-Opa1 for 0.2 mg liposome) and incubated for 2
463 hours. Surfactant was removed by dialysis overnight under 4 °C using a 3.5 KDa dialysis
464 cassette. Excess calcein was removed using a PD-10 desalting column. The final concentration
465 of liposome was determined by TexasRed absorbance, measured in a SpectraMax i3 plate reader
466 (Molecular Devices).

467

468 To evaluate l-Opa1 reconstitution into proteoliposomes, dye free liposome was prepared with
469 TexasRed conjugated anti-His tag Antibody (ThermoFisher) by mixing lipids with antibody
470 containing buffer. TexasRed Labeling efficiency of the antibody was calculated to be 1.05
471 according to the vendor's protocol. Antibodies were added at a concentration of 2.6 µg/ml to 0.2

472 mg/ml liposome. Following hydration through vortexing at room temperature for 15 minutes,
473 Large unilamellar vesicles were formed following 20 times extrusion procedure described above.
474 Liposomes labeled with 0.02 % (mol) TexasRed-PE were also prepared as a standard for
475 quantifying reconstitution rate.

476

477 For the co-flootation analysis, 200 μ l of 20 mg/ml TexasRed-DHPE (0.2 % (mol)) labeled
478 proteoliposome (reconstitution ratio, protein:lipid 1:5000) was loaded to sucrose gradient (with
479 steps of 0%, 15%, 30%, 60%). The volume of each fraction was 800 μ l. Sucrose solutions were
480 prepared in Bis-Tris buffer (25mM Bis-Tris, 150 mM NaCl, pH 7.4). Samples were then
481 centrifuged using a high-speed centrifuge equipped with SW 55i rotor (Beckmann Coulter, CA,
482 USA) for 2.5 hrs at a speed of 30000 xg. For high salt and carbonate treatment, the same amount
483 of proteoliposome was redistributed in Bis-Tris buffer with 500 mM NaCl (pH 7.4) and buffer
484 containing 50 mM Na₂CO₃ and 50 mM NaCl (pH 8.2), respectively. The resulting suspension
485 was loaded in gradient for separation. After centrifugation, all fractions were collected and
486 concentrated to 40 μ l. Fractions were detected by western blot and then analyzed by ImageJ. The
487 presence of liposomes was detected by absorbance at 590 nm using a DeNovix FX photometer
488 (DeNovix, Inc).

489

490 **Fluorescent Correlation Spectroscopy**

491 Fluorescence correlation spectroscopy (FCS) was performed using a home-built PIE-FCCS
492 system (52, 53). Two pulsed laser beams with wavelengths of 488 nm (9.7 MHz, 5 ps) and 561
493 nm (9.7 MHz, 5 ps) were filtered out from a supercontinuum white light fiber laser (SuperK
494 NKT Photonics, Birkerod, Denmark) and used as excitation beams. The laser beams were sent
495 through a 100X TIRF objective (NA 1.47, oil, Nikon Corp., Tokyo, Japan) to excite the samples
496 in solution or on bilayer. The emission photons were guided through a common 50 μ m diameter
497 pinhole. The light was spectrally separated by a 560 nm high-pass filter (AC254-100-A-ML,
498 Thorlabs), further filtered by respective bandpass filters (green, 520/44 nm [FF01-520/44-25];
499 red, 612/69 nm [FF01-621/69-25], Semrock), and finally reach two single photon avalanche
500 diode (SPAD) detectors (Micro Photon Devices). The synchronized photon data was collected
501 using a time correlated single photon counting (TCSPC) module (PicoHarp 300, PicoQuant,
502 Berlin, Germany).

503
504 The collected photon data was transformed into correlation functions with a home written
505 MATLAB code. The correlation functions were fitted using two-dimensional (1) or three-
506 dimensional (2) Brownian diffusion model for bilayer or solution samples respectively.

507
508 $G(\tau) = \frac{1}{\langle N \rangle} \frac{1}{1+\tau/\tau_D}$ (1)
509 $G(\tau) = \frac{1}{\langle N \rangle} \frac{1}{1+\tau/\tau_D} \frac{1}{\sqrt{1+\omega^2 \cdot \frac{\tau}{\tau_D}}}$ (2)

510
511 Where N is the average number of particles in the system, ω is the waist of the excitation beam,
512 and τ_D is the dwell time that can be used to calculate the diffusion coefficient (D) of the particles.
513

$$\tau_D = \frac{\omega^2}{4D}$$

514 (52)

515
516 Measurements were made on buffers with evenly distributed liposomes, proteoliposomes and
517 antibodies in a glass-bottom 96 well plate at room temperature. The plates were pre-coated with
518 lipid bilayer fabricated from 100 nm DOPC liposomes. For each solution, data was collected in
519 five successive 15 second increments.

520
521 For characterization of 1-Opa1 reconstitution into planar bilayers, an anti-Opa1 C-terminal
522 antibody (Novus Biologicals, CO, USA) was used. The antibody was labeled by TexasRed
523 (Texas Red™-X Protein Labeling Kit, ThermoFisher, CA, USA). Labeling efficiency of the
524 antibody was determined as 1.52 TexasRed/antibody, as determined by NanoDrop
525 (ThermoFisher, CA, USA). The labeled antibody was added to 1-Opa1 in the supported bilayer at
526 twice the total introduced Opa1 concentration. Excess antibody was removed by extensive
527 rinsing.

528
529 To estimate reconstitution efficiency, 0.002 % (mol) 1-Opa1 was added to the bilayer. In a
530 separate experiment 0.002 % (mol) TexasRed-PE was introduced to the bilayer. The

531 reconstitution efficiency was calculated from the anti-l-Opa1 antibody TexasRed fluorophore
532 density divided by the TexasRed-PE fluorophore density, normalized by the antibody labeling
533 efficiency (1.5 dye molecules/antibody).

534

535 **Total Internal Reflection Fluorescent Microscopy (TIRF)**

536 Liposome docking and lipid exchange events were imaged using a Vector TIRF system
537 (Intelligent Imaging Innovations, Inc, Denver, CO, USA) equipped with a W-view Gemini
538 system (Hamamatsu photonics, Bridgewater, NJ). TIRF images were acquired using a 100X oil
539 immersion objective (Ziess, N.A 1.4). A 543 nm laser was used for the analysis of TexasRed-PE
540 embedded liposomes and proteoliposomes, while a 633 nm laser was applied for the analysis of
541 Cy5-PE embedded in the planar lipid bilayer. Fluorescent emission was simultaneously observed
542 through a 609-emission filter with a band width of 40 nm and a 698-emission filter with a band
543 width of 70 nm. The microscope system was equipped with a Prime 95B scientific CMOS
544 camera (Photometrics), maintained at -10 °C. Images were taken at room temperature, before
545 adding any liposome or proteoliposome, after 15 mins of addition, and after 30 mins of adding
546 GTP (1 mM) and MgCl₂(1 mM). Each data point was acquired from 5 different bilayers, each
547 bilayer data contains 5-10 particles on average.

548

549 Dwell times for hemifused particles were recorded from the moment of GTP addition for pre-
550 tethered particles, until the time of half-maximal TexasRed signal decay. Full fusion events were
551 recorded by monitoring the calcein channel at particle locations identified through the TexasRed
552 signal. Particle identification and localization used both uTrack(54) and Slidebook (Intelligent
553 Imaging Innovations, Inc., Denver, CO) built-in algorithms. To calibrate the point spread
554 function 100 nm and 50 nm fluorescent particles (ThermoFisher Scientific) were used. 2D
555 Gaussian detection were applied in both cases. 2-way ANOVA tests was done using GraphPad
556 Prism. Intensity and distribution of the particles were analyzed using ImageJ.

557

558 For analysis of protein reconstitution in proteoliposome (stoichiometry), a TIRF microscope
559 modified from an inverted microscope (Nikon Eclipse Ti, Nikon Instruments) was used. A 561
560 nm diode laser (OBIS, Coherent Inc., Santa Clara, USA) was applied at TIRF angle through a

561 100X TIRF objective (NA 1.47, oil, Nikon) and the fluorescence signals were collected by an
562 EMCCD camera (Evolve 512, Photometrics).

563

564 **Nanosight NTA analysis**

565 A NTA300 Nanosight instrument was used to evaluate size distribution of liposome and
566 proteoliposome under different conditions. The equipment was equipped with a 405 nm laser and
567 a CMOS camera. 1 ml of 0.1 µg/ml sample was measured, to reach the recommended particle
568 number of 1×10^8 particles/mL (corresponding to the dilution factor of 1:100,000). Image
569 acquisition were conducted for 40 sec for each acquisition and repeated for 10 times for every
570 injection. Three parallel samples were examined for the determination of size distribution. Under
571 each run, the camera level was set to 12 and the detection threshold was set at 3.

572

573 **Blue native polyacrylamide gel electrophoresis (BN-PAGE)**

574 Bis-Tris gradient gels (3-12%) were purchased from ThermoFisher Scientific (Cat. No.
575 BN1003BOX) and BN-PAGE was performed according to manufacturer's instructions. Gel
576 samples (10 µl) were prepared by mixing indicated quantity of Opa1 with sample buffer
577 containing 0.25% Coomassie G-250 and 1 mM DDM. For experiments involving l-Opa1 and s-
578 Opa1 mixtures, the samples were incubated on ice for 10 min before loading. The cathode buffer
579 contained 1 mM DDM and electrophoresis was performed at 4°C with an ice jacket surrounding
580 the apparatus.

581

582 **Figure Legends**

583

584 **Figure 1**

585 A. Mitochondrial membrane fusion involves sequential outer and inner membrane fusion. The
586 mitofusins (Mfn1/2) catalyze outer membrane fusion. In metazoans, mitochondrial inner-
587 membrane fusion is mediated by Opa1. B. Linear domain arrangement of l-Opa1. C. Schema of
588 the experimental setup. D. Fusion assay. Membrane tethering, docking, lipid mixing, and content
589 release can be distinguished using fluorescent reporters that specifically reflect each transition of
590 the reaction.

591

592 **Figure 2**

593 A. Representative size-exclusion chromatograph and SDS-PAGE gel of human l-Opa1 purified
594 from *P. pastoris*. B. SDS-PAGE gel of human s-Opa1 purified from *P. pastoris*. l-Opa1 activity,
595 with velocity (C) and specific activity (D) of GTP hydrolysis in the presence and absence of
596 cardiolipin, while varying protein concentration of Opa1. Data are shown as mean ± SD, with
597 error bars from 3 independent experiments. Representative single-liposome photobleaching steps
598 (E & F) and histogram of step sizes (distribution for 110 liposomes shown) (G). Source data:
599 Figure2-source data1.zip

600

601 **Figure 2 – figure supplement 1**

602 GTP hydrolysis (GTPase) activity of l-Opa1 (A) and s-Opa1 (B) in the presence and absence of
603 cardiolipin. Both G300E l-Opa1 and G300E s-Opa1 do not show any GTPase activity (C & D).
604 Mixing G300E s-Opa1 with WT l-Opa1 at 1:1 molar ratio (E) does not alter the GTPase activity
605 of, detergent solubilized, WT l-Opa1 significantly (E and A, P>0.2, t-test). A similar effect is
606 seen upon addition of G300E l-Opa1 to WT s-Opa1 at 1:1 ratio (F). Under these conditions, s-
607 Opa1 GTPase activity is similar to s-Opa1 alone (F & B, P>0.2, t-test). Data shown as mean ±
608 SD, error bars from 3 experiments. Source data: Figure 2-fig sup 1-source data1.zip

609

610 **Figure 2 – figure supplement 2**

611 Liposome co-flootation analysis: Reconstituted l-Opa1 co-floats with liposomes both with and
612 without cardiolipin (A & D). Liposomes were labeled with 0.2 % (mol) TexasRed-DHPE and
613 their distribution was confirmed by liposome dye absorbance at 590 nm. Opa1 distribution was
614 analyzed by Western blot. Opa1/liposome fractions was mostly found near 15~30% sucrose.
615 This reconstitution is stable under high salt (B & E) or carbonate conditions (C & F). s-Opa1
616 interacts with liposomes in a cardiolipin-dependent manner (G-L). This interaction is resistant to
617 high salt (H) but sensitive to carbonate treatment (I), where the protein was found in the bottom
618 fractions lacking liposome (60% sucrose). s-Opa1 does not associate with DOPC liposomes (J-
619 L). These results indicate that l-Opa1 was successfully reconstituted through integral
620 transmembrane region, whereas the s-Opa1 bilayer-association is through a cardiolipin:s-Opa1
621 peripheral membrane interaction. Source data: Figure 2-fig sup 2-source data1.zip

622

623 **Figure 2 – figure supplement 3**

624 Epifluorescence image of polymer-tethered lipid bilayers before (A) and after Opa1
625 reconstitution (B), showing a homogeneous lipid bilayer. Scale bar: 10 μ m. FCS profiles of
626 TexasRed-PE and TexasRed labeled anti-Opa1 antibody show slower diffusion for reconstituted
627 l-Opa1 (C), indicating successful reconstitution, and that the reconstituted l-Opa1 diffuses freely.
628 Source data: Figure 2-fig sup 3-source data1.zip

629

630 **Figure 2 – figure supplement 4**

631 A. Blue native (BN-PAGE) gels show WT l-Opa1 and s-Opa1 can self-assemble as oligomers in
632 DDM. B. Mixtures of WT l-Opa1 and WT s-Opa1 show a range of species from ~480 KDa - ~1
633 MDa. G300E l-Opa1, in the presence of WT s-Opa1, does not alter this gel migration pattern. In
634 contrast, complexes comprising WT l-Opa1 and G300E s-Opa1 show a slight shift to a
635 population mainly containing a ~480 Kda and 720 KDa species.

636

637 **Figure 2 – figure supplement 5**

638 Fluorescence autocorrelation profiles of TexasRed labeled anti-His antibody in the presence of
639 unlabeled liposomes (A), and TexasRed-PE-labeled liposomes (B), showing diffusion
640 coefficients of unbound antibody versus liposomes. FCS profile of reconstituted l-Opa1 (detected

641 with a TexasRed labeled antibody) (C) is similar to that of dye-labeled liposomes (B), indicating
642 successful reconstitution of Opa1. Source data: Figure 2-fig sup 5-source data1.zip

643

644 **Figure 3**

645 The number of liposomes tethered on the planar bilayers in a homotypic format (l-Opa1 on both
646 bilayers) increases in the presence of GTP, when both bilayers contain cardiolipin. A.
647 Representative images of liposomes tethered on lipid bilayer (both containing cardiolipin) before
648 (apo, or nucleotide free) and after GTP addition. Scale bar: 5 μ m. B. Bar graph: In the presence of
649 cardiolipin, addition of GTP doubles the number of liposomes. (***p<0.001, two way
650 ANOVA). C. Addition of GMPPCP decreases amount of tethered l-Opa1 liposomes (apo,
651 indicating nucleotide free) (P<0.005, two-way ANOVA). D. l-Opa1 in the liposome bilayer
652 alone is sufficient to tether liposomes to a cardiolipin containing bilayer. Tethering is enhanced
653 in the presence of GTP (apo, indicating nucleotide free) (P<0.005, two-way ANOVA). E. s-Opa1
654 tethers liposomes to a cardiolipin-containing bilayer. Number of tethered liposomes when both
655 bilayer and liposomes contain 20% (mol) cardiolipin. Before addition of GTP (apo, indicating
656 nucleotide-free), a moderate amount of liposome tethering was observed. The addition of GTP
657 enhances this tethering effect (P<0.005, two-way ANOVA). Data are shown as mean \pm SD. Error
658 bars are from 5 independent experiments (> 10 images across one bilayer per for each
659 experiment). Source data: Figure 3-source data1.zip

660

661 **Figure 3 – figure supplement 1**

662 Effect of s-Opa1 competition on membrane tethering. Addition of G300E s-Opa1 detaches the l-
663 Opa1 proteoliposomes tethered to l-Opa1-containing supported lipid (A). G300E l-Opa1 does not
664 tether liposomes to a supported bilayer (B). G300E l-Opa1 in the presence of G300E s-Opa1 also
665 does not tether membranes. Addition of WT s-Opa1 to G300E l-Opa1 proteoliposomes and a l-
666 Opa1-containing supported lipid tethers liposomes (A). Source data: Figure 3-fig sup 1-source
667 data1.zip

668

669 **Figure 3 – figure supplement 2**

670 Normalized relative and cumulative size distributions show cardiolipin containing
671 proteoliposomes shift to larger sizes 1 hour following GTP addition (green trace), as measured
672 by Nanosight light scattering. Source data: Figure 3-fig sup 2-source data1.zip

673

674 **Figure 4**

675 A. Homotypic l-Opa1 docks liposomes in a GTP-hydrolysis dependent manner. s-Opa1, alone is
676 insufficient to closely dock liposomes. l-Opa1 in a heterotypic format (on the liposome alone) is
677 competent to closely dock to a bilayer, but this docking is not stimulated by nucleotide. Bar
678 graphs shown as mean \pm SD ($P<0.0001$, one-way ANOVA). Error bars are from 3-5 independent
679 experiments (each experiment with >150 particles in a given bilayer). B. In the presence of
680 cardiolipin on both bilayers, FRET signal reports on close liposome docking mediated by l-
681 Opa1. Left: Green = Cy5 emission signal upon excitation at 543 (TexasRed excitation). Red =
682 Cy5 emission signal in membrane upon excitation at 633 (Cy5 excitation). Right: Green =
683 TexasRed emission upon excitation at 543 nm (TexasRed excitation). Scale bar: 5 μ m. Source
684 data: Figure 4- source data1.zip

685

686 **Figure 4 – figure supplement 1**

687 A. Controls for intra-membrane and inter-membrane FRET: When both TexasRed and Cy5 PE
688 are present in the same bilayer, high FRET efficiency is observed. When TexasRed and Cy5 PE
689 are present in two different bilayers, with a ~7 nm tethering distance (from bilayer center to
690 bilayer center in the double bilayer stack), FRET efficiency was low (data analyzed from 10
691 random spots in 2 bilayers ($P<0.0001$, t test). Analysis of ~20 particles show ~40% FRET
692 efficiency for both homotypic and heterotypic tethering. This indicates that l-Opa1 is able to
693 bring the two membranes within close proximity (< 7 nm) without mixing the two membranes.
694 B. Quantification of DOPC liposomes tethered to a DOPC bilayer containing reconstituted l-
695 Opa1. Liposomes do not tether to the supported bilayer, indicating that in the absence of
696 cardiolipin, l-Opa1 does not tether liposomes alone. The lack of liposome docking to exposed
697 regions also argues that few defects were introduced into the bilayer following reconstitution.
698 Data from 3 different bilayers. Source data: Figure 4-fig sup 1-source data1.zip

699

700 **Figure 5**
701 A. Heterotypic hemifusion. Top panels: time trace of proteo-liposome lipid dye diffusion
702 (TexasRed). Bottom panels: no content release is observed for this particle (calcein signal
703 remains quenched). Scale bar: 1 μ m. B. Homotypic hemifusion. Top panels: time trace of
704 liposome lipid dye diffusion (TexasRed). Bottom panels: no content release is observed for this
705 particle (calcein signal remains quenched). Scale bar: 1 μ m. C. Representative intensity traces of
706 a control particle not undergoing fusion (black), with heterotypic hemifusion event (solid red),
707 and homotypic hemifusion event (dotted red). Source data: Figure 5-source data1.zip
708

709 **Figure 5 – figure supplement 1**
710 Additional kinetic traces for hemifusion curves under homotypic (A) and heterotypic (B) Opa1
711 hemifusion conditions. Control particle trace shown in black. Hemifusion trace shown in red.
712 Source data: Figure 5-fg sup 1-source data1.zip
713

714 **Figure 6**
715 A. Hemifusion (lipid mixing) and full fusion (content release and pore opening) efficiency for
716 homotypic l-Opa1, heterotypic l-Opa1 and s-Opa1 ($P<0.001$, two-way ANOVA). Bar graphs
717 shown as mean \pm SD. Error bars are from 5 different experiments (50-200 particles were
718 analyzed per bilayer in each experiment). B. Full fusion (pore opening) efficiency at different s-
719 Opa1:l-Opa1 ratios. Data is shown as mean \pm SD. Error bars are from 4-6 experiments (80-150
720 particles per bilayer in each experiment). The significance of the data was confirmed using one-
721 way ANOVA (Prism 8.3) where $P<0.0001$. C. Mean pore opening time in the absence of s-Opa1
722 and at equimolar s-Opa1. Significance of the difference was confirmed using t-test (Prism 8.3,
723 $P<0.0001$). D. Representative hemifusion and pore opening fluorescence time series for
724 homotypic l-Opa1 experiment, in the absence of s-Opa1, top and bottom panels, respectively.
725 Scale bar: 1 μ m. E: representative traces of TexasRed (liposome signal) and calcein (content
726 signal) intensity for homotypic l-Opa1 experiment. F. Representative hemifusion and pore
727 opening fluorescence traces for a homotypic l-Opa1 experiment in the presence of equimolar s-
728 Opa1. Scale bar: 1 μ m. G: Representative trace of TexasRed (liposome signal) and calcein
729 (content signal) intensity for a homotypic l-Opa1 experiment in the presence of equimolar s-
730 Opa1. Source data: Figure 6-source data1.zip

731

732 **Figure 6 – figure supplement 1**

733 Additional kinetic traces for hemifusion and pore opening under homotypic l-Opa1 conditions
734 (A), homotypic l-Opa1, and l-Opa1 + s-Opa1 (1:1) (B) conditions. Hemifusion (TexasRed) trace
735 show in red. Pore opening (calcein, content release) trace shown in green. Figure 6-fig sup1-
736 source data1.zip

737

738 **Figure 7**

739 Summary model for modes of regulation in Opal-mediated membrane fusion. A. s-Opa1 alone is
740 capable of tethering bilayers, but insufficient for close membrane docking and hemifusion. B. l-
741 Opa1, in a heterotypic arrangement, can tether bilayers, and upon GTP stimulation promote low
742 levels of lipid mixing, but no full fusion, pore opening or content release. C. Homotypic l-Opa1-
743 l-Opa1 tethered bilayers can mediate full content release (i). This activity is greatly stimulated by
744 the presence of s-Opa1, with peak activity at 1:1 s-Opa1:l-Opa1 (ii). Excess levels of s-Opa1
745 suppress fusion, likely through competing with the l-Opa1-l-Opa1 homotypic tethering interface
746 (iii).

747

748

749 **References**

- 750 1. Hoppins S, Lackner L, Nunnari J. The machines that divide and fuse mitochondria. *Annu
751 Rev Biochem.* 2007;76:751-80. Epub 2007/03/17. doi:
752 10.1146/annurev.biochem.76.071905.090048. PubMed PMID: 17362197.
- 753 2. Cipolat S, Rudka T, Hartmann D, Costa V, Serneels L, Craessaerts K, Metzger K, Frezza C,
754 Annaert W, D'Adamio L, Derkx C, Dejaegere T, Pellegrini L, D'Hooge R, Scorrano L, De Strooper
755 B. Mitochondrial rhomboid PARL regulates cytochrome c release during apoptosis via OPA1-
756 dependent cristae remodeling. *Cell.* 2006;126(1):163-75. Epub 2006/07/15. doi:
757 10.1016/j.cell.2006.06.021. PubMed PMID: 16839884.
- 758 3. Cogliati S, Frezza C, Soriano ME, Varanita T, Quintana-Cabrera R, Corrado M, Cipolat S,
759 Costa V, Casarin A, Gomes LC, Perales-Clemente E, Salviati L, Fernandez-Silva P, Enriquez JA,
760 Scorrano L. Mitochondrial cristae shape determines respiratory chain supercomplexes assembly
761 and respiratory efficiency. *Cell.* 2013;155(1):160-71. Epub 2013/09/24. doi:
762 10.1016/j.cell.2013.08.032. PubMed PMID: 24055366; PMCID: PMC3790458.
- 763 4. Nunnari J, Suomalainen A. Mitochondria: in sickness and in health. *Cell.*
764 2012;148(6):1145-59. doi: 10.1016/j.cell.2012.02.035. PubMed PMID: 22424226; PMCID:
765 PMC5381524.
- 766 5. Westermann B. Mitochondrial fusion and fission in cell life and death. *Nat Rev Mol Cell
767 Biol.* 2010;11(12):872-84. doi: 10.1038/nrm3013. PubMed PMID: 21102612.
- 768 6. Anand R, Wai T, Baker MJ, Kladt N, Schauss AC, Rugarli E, Langer T. The i-AAA protease
769 YME1L and OMA1 cleave OPA1 to balance mitochondrial fusion and fission. *J Cell Biol.*
770 2014;204(6):919-29. doi: 10.1083/jcb.201308006. PubMed PMID: 24616225; PMCID:
771 PMC3998800.
- 772 7. Chen H, Detmer SA, Ewald AJ, Griffin EE, Fraser SE, Chan DC. Mitofusins Mfn1 and Mfn2
773 coordinately regulate mitochondrial fusion and are essential for embryonic development. *J Cell
774 Biol.* 2003;160(2):189-200. Epub 2003/01/16. doi: 10.1083/jcb.200211046. PubMed PMID:
775 12527753; PMCID: PMC2172648.
- 776 8. Alexander C, Votruba M, Pesch UE, Thiselton DL, Mayer S, Moore A, Rodriguez M,
777 Kellner U, Leo-Kottler B, Auburger G, Bhattacharya SS, Wissinger B. OPA1, encoding a dynamin-
778 related GTPase, is mutated in autosomal dominant optic atrophy linked to chromosome 3q28.
779 *Nat Genet.* 2000;26(2):211-5. Epub 2000/10/04. doi: 10.1038/79944. PubMed PMID: 11017080.
- 780 9. Meeusen S, DeVay R, Block J, Cassidy-Stone A, Wayson S, McCaffery JM, Nunnari J.
781 Mitochondrial inner-membrane fusion and crista maintenance requires the dynamin-related
782 GTPase Mgm1. *Cell.* 2006;127(2):383-95. Epub 2006/10/24. doi: 10.1016/j.cell.2006.09.021.
783 PubMed PMID: 17055438.
- 784 10. Meeusen S, McCaffery JM, Nunnari J. Mitochondrial fusion intermediates revealed in
785 vitro. *Science.* 2004;305(5691):1747-52. Epub 2004/08/07. doi: 10.1126/science.1100612.
786 PubMed PMID: 15297626.
- 787 11. MacVicar T, Langer T. OPA1 processing in cell death and disease - the long and short of
788 it. *J Cell Sci.* 2016;129(12):2297-306. Epub 2016/05/18. doi: 10.1242/jcs.159186. PubMed PMID:
789 27189080.
- 790 12. Olichon A, Baricault L, Gas N, Guillou E, Valette A, Belenguer P, Lenaers G. Loss of OPA1
791 perturbs the mitochondrial inner membrane structure and integrity, leading to cytochrome c

- 792 release and apoptosis. *J Biol Chem.* 2003;278(10):7743-6. Epub 2003/01/02. doi:
793 10.1074/jbc.C200677200. PubMed PMID: 12509422.
- 794 13. Pesch UE, Leo-Kottler B, Mayer S, Jurklies B, Kellner U, Apfelstedt-Sylla E, Zrenner E,
795 Alexander C, Wissinger B. OPA1 mutations in patients with autosomal dominant optic atrophy
796 and evidence for semi-dominant inheritance. *Hum Mol Genet.* 2001;10(13):1359-68. Epub
797 2001/07/07. doi: 10.1093/hmg/10.13.1359. PubMed PMID: 11440988.
- 798 14. Schmid SL, Frolov VA. Dynamin: functional design of a membrane fission catalyst. *Annu
799 Rev Cell Dev Biol.* 2011;27:79-105. doi: 10.1146/annurev-cellbio-100109-104016. PubMed
800 PMID: 21599493.
- 801 15. Ramachandran R, Schmid SL. The dynamin superfamily. *Curr Biol.* 2018;28(8):R411-R6.
802 doi: 10.1016/j.cub.2017.12.013. PubMed PMID: 29689225.
- 803 16. Faelber K, Dietrich L, Noel JK, Wollweber F, Pfitzner AK, Muhleip A, Sanchez R,
804 Kudryashev M, Chiaruttini N, Lilie H, Schlegel J, Rosenbaum E, Hessenberger M, Matthaeus C,
805 Kunz S, von der Malsburg A, Noe F, Roux A, van der Laan M, Kuhlbrandt W, Daumke O.
806 Structure and assembly of the mitochondrial membrane remodelling GTPase Mgm1. *Nature.*
807 2019. doi: 10.1038/s41586-019-1372-3. PubMed PMID: 31292547.
- 808 17. Faelber K, Posor Y, Gao S, Held M, Roske Y, Schulze D, Haucke V, Noe F, Daumke O.
809 Crystal structure of nucleotide-free dynamin. *Nature.* 2011;477(7366):556-60. Epub
810 2011/09/20. doi: 10.1038/nature10369. PubMed PMID: 21927000.
- 811 18. Mishra P, Carelli V, Manfredi G, Chan DC. Proteolytic cleavage of Opa1 stimulates
812 mitochondrial inner membrane fusion and couples fusion to oxidative phosphorylation. *Cell
813 Metab.* 2014;19(4):630-41. doi: 10.1016/j.cmet.2014.03.011. PubMed PMID: 24703695; PMCID:
814 PMC4018240.
- 815 19. Ehses S, Raschke I, Mancuso G, Bernacchia A, Geimer S, Tonnerer D, Martinou JC,
816 Westermann B, Rugarli EI, Langer T. Regulation of OPA1 processing and mitochondrial fusion by
817 m-AAA protease isoforms and OMA1. *J Cell Biol.* 2009;187(7):1023-36. Epub 2009/12/30.
818 doi: 10.1083/jcb.200906084. PubMed PMID: 20038678; PMCID: PMC2806285.
- 819 20. Ban T, Heymann JA, Song Z, Hinshaw JE, Chan DC. OPA1 disease alleles causing
820 dominant optic atrophy have defects in cardiolipin-stimulated GTP hydrolysis and membrane
821 tubulation. *Hum Mol Genet.* 2010;19(11):2113-22. doi: 10.1093/hmg/ddq088. PubMed PMID:
822 20185555; PMCID: PMC2865371.
- 823 21. Frezza C, Cipolat S, Martins de Brito O, Micaroni M, Beznoussenko GV, Rudka T, Bartoli
824 D, Polishuck RS, Danial NN, De Strooper B, Scorrano L. OPA1 controls apoptotic cristae
825 remodeling independently from mitochondrial fusion. *Cell.* 2006;126(1):177-89. Epub
826 2006/07/15. doi: 10.1016/j.cell.2006.06.025. PubMed PMID: 16839885.
- 827 22. Ford MG, Jenni S, Nunnari J. The crystal structure of dynamin. *Nature.* 2011;477(7366):561-6.
828 Epub 2011/09/20. doi: 10.1038/nature10441. PubMed PMID: 21927001; PMCID: PMC4075756.
- 829 23. Antonny B, Burd C, De Camilli P, Chen E, Daumke O, Faelber K, Ford M, Frolov VA, Frost
830 A, Hinshaw JE, Kirchhausen T, Kozlov MM, Lenz M, Low HH, McMahon H, Merrifield C, Pollard
831 TD, Robinson PJ, Roux A, Schmid S. Membrane fission by dynamin: what we know and what we
832 need to know. *EMBO J.* 2016;35(21):2270-84. Epub 2016/11/04. doi:
833 10.15252/embj.201694613. PubMed PMID: 27670760; PMCID: PMC5090216.

- 835 24. Chappie JS, Acharya S, Leonard M, Schmid SL, Dyda F. G domain dimerization controls
836 dynamin's assembly-stimulated GTPase activity. *Nature*. 2010;465(7297):435-40. Epub
837 2010/04/30. doi: 10.1038/nature09032. PubMed PMID: 20428113; PMCID: PMC2879890.
- 838 25. DeVay RM, Dominguez-Ramirez L, Lackner LL, Hoppins S, Stahlberg H, Nunnari J.
839 Coassembly of Mgm1 isoforms requires cardiolipin and mediates mitochondrial inner
840 membrane fusion. *J Cell Biol*. 2009;186(6):793-803. doi: 10.1083/jcb.200906098. PubMed
841 PMID: 19752025; PMCID: PMC2753158.
- 842 26. Herlan M, Vogel F, Bornhovd C, Neupert W, Reichert AS. Processing of Mgm1 by the
843 rhomboid-type protease Pcp1 is required for maintenance of mitochondrial morphology and of
844 mitochondrial DNA. *J Biol Chem*. 2003;278(30):27781-8. Epub 2003/04/23. doi:
845 10.1074/jbc.M211311200. PubMed PMID: 12707284.
- 846 27. Song Z, Chen H, Fiket M, Alexander C, Chan DC. OPA1 processing controls mitochondrial
847 fusion and is regulated by mRNA splicing, membrane potential, and Yme1L. *J Cell Biol*.
848 2007;178(5):749-55. Epub 2007/08/22. doi: 10.1083/jcb.200704110. PubMed PMID: 17709429;
849 PMCID: PMC2064540.
- 850 28. Ban T, Ishihara T, Kohno H, Saita S, Ichimura A, Maenaka K, Oka T, Mihara K, Ishihara N.
851 Molecular basis of selective mitochondrial fusion by heterotypic action between OPA1 and
852 cardiolipin. *Nat Cell Biol*. 2017;19(7):856-63. doi: 10.1038/ncb3560. PubMed PMID: 28628083.
- 853 29. Del Dotto V, Fogazza M, Carelli V, Rugolo M, Zanna C. Eight human OPA1 isoforms, long
854 and short: What are they for? *Biochim Biophys Acta Bioenerg*. 2018;1859(4):263-9. Epub
855 2018/02/01. doi: 10.1016/j.bbabi.2018.01.005. PubMed PMID: 29382469.
- 856 30. Naumann C, Prucker O, Lehmann T, Ruhe J, Knoll W, Frank CW. The polymer-supported
857 phospholipid bilayer: tethering as a new approach to substrate-membrane stabilization.
858 *Biomacromolecules*. 2002;3(1):27-35. Epub 2002/02/28. PubMed PMID: 11866552.
- 859 31. Siegel AP, Kimble-Hill A, Garg S, Jordan R, Naumann CA. Native ligands change integrin
860 sequestering but not oligomerization in raft-mimicking lipid mixtures. *Biophys J*.
861 2011;101(7):1642-50. Epub 2011/10/04. doi: 10.1016/j.bpj.2011.08.040. PubMed PMID:
862 21961590; PMCID: PMC3183796.
- 863 32. Liu TY, Bian X, Romano FB, Shemesh T, Rapoport TA, Hu J. Cis and trans interactions
864 between atlastin molecules during membrane fusion. *Proc Natl Acad Sci U S A*.
865 2015;112(15):E1851-60. Epub 2015/04/01. doi: 10.1073/pnas.1504368112. PubMed PMID:
866 25825753; PMCID: PMC4403200.
- 867 33. O'Donnell JP, Cooley RB, Kelly CM, Miller K, Andersen OS, Rusinova R, Sondermann H.
868 Timing and Reset Mechanism of GTP Hydrolysis-Driven Conformational Changes of Atlastin.
869 Structure. 2017;25(7):997-1010 e4. Epub 2017/06/13. doi: 10.1016/j.str.2017.05.007. PubMed
870 PMID: 28602821; PMCID: PMC5516944.
- 871 34. Abutbul-Ionita I, Rujiviphat J, Nir I, McQuibban GA, Danino D. Membrane tethering and
872 nucleotide-dependent conformational changes drive mitochondrial genome maintenance
873 (Mgm1) protein-mediated membrane fusion. *J Biol Chem*. 2012;287(44):36634-8. Epub
874 2012/09/15. doi: 10.1074/jbc.C112.406769. PubMed PMID: 22977249; PMCID: PMC3481265.
- 875 35. Chao LH, Klein DE, Schmidt AG, Pena JM, Harrison SC. Sequential conformational
876 rearrangements in flavivirus membrane fusion. *Elife*. 2014;3:e04389. Epub 2014/12/06. doi:
877 10.7554/eLife.04389. PubMed PMID: 25479384; PMCID: PMC4293572.

- 878 36. Ivanovic T, Choi JL, Whelan SP, van Oijen AM, Harrison SC. Influenza-virus membrane
879 fusion by cooperative fold-back of stochastically induced hemagglutinin intermediates. *Elife*.
880 2013;2:e00333. Epub 2013/04/04. doi: 10.7554/elife.00333. PubMed PMID: 23550179; PMCID:
881 PMC3578201.
- 882 37. Rawle RJ, van Lengerich B, Chung M, Bendix PM, Boxer SG. Vesicle fusion observed by
883 content transfer across a tethered lipid bilayer. *Biophys J*. 2011;101(8):L37-9. Epub 2011/10/19.
884 doi: 10.1016/j.bpj.2011.09.023. PubMed PMID: 22004762; PMCID: PMC3192961.
- 885 38. Gripasic L, Kanazawa T, van der Bliek AM. Regulation of the mitochondrial dynamin-like
886 protein Opa1 by proteolytic cleavage. *J Cell Biol*. 2007;178(5):757-64. Epub 2007/08/22. doi:
887 10.1083/jcb.200704112. PubMed PMID: 17709430; PMCID: PMC2064541.
- 888 39. Lee H, Smith SB, Yoon Y. The short variant of the mitochondrial dynamin OPA1
889 maintains mitochondrial energetics and cristae structure. *J Biol Chem*. 2017;292(17):7115-30.
890 doi: 10.1074/jbc.M116.762567. PubMed PMID: 28298442; PMCID: PMC5409478.
- 891 40. Baker MJ, Lampe PA, Stojanovski D, Korwitz A, Anand R, Tatsuta T, Langer T. Stress-
892 induced OMA1 activation and autocatalytic turnover regulate OPA1-dependent mitochondrial
893 dynamics. *EMBO J*. 2014;33(6):578-93. doi: 10.1002/embj.201386474. PubMed PMID:
894 24550258; PMCID: PMC3989652.
- 895 41. Brandt T, Cavellini L, Kuhlbrandt W, Cohen MM. A mitofusin-dependent docking ring
896 complex triggers mitochondrial fusion in vitro. *Elife*. 2016;5. Epub 2016/06/03. doi:
897 10.7554/elife.14618. PubMed PMID: 27253069; PMCID: PMC4929004.
- 898 42. Zick M, Duvezin-Caubet S, Schafer A, Vogel F, Neupert W, Reichert AS. Distinct roles of
899 the two isoforms of the dynamin-like GTPase Mgm1 in mitochondrial fusion. *FEBS Lett*.
900 2009;583(13):2237-43. Epub 2009/06/10. doi: 10.1016/j.febslet.2009.05.053. PubMed PMID:
901 19505460.
- 902 43. Wai T, Langer T. Mitochondrial Dynamics and Metabolic Regulation. *Trends Endocrinol
903 Metab*. 2016;27(2):105-17. doi: 10.1016/j.tem.2015.12.001. PubMed PMID: 26754340.
- 904 44. Duvezin-Caubet S, Jagasia R, Wagener J, Hofmann S, Trifunovic A, Hansson A, Chomyn A,
905 Bauer MF, Attardi G, Larsson NG, Neupert W, Reichert AS. Proteolytic processing of OPA1 links
906 mitochondrial dysfunction to alterations in mitochondrial morphology. *J Biol Chem*.
907 2006;281(49):37972-9. Epub 2006/09/28. doi: 10.1074/jbc.M606059200. PubMed PMID:
908 17003040.
- 909 45. Rainbolt TK, Lebeau J, Puchades C, Wiseman RL. Reciprocal Degradation of YME1L and
910 OMA1 Adapts Mitochondrial Proteolytic Activity during Stress. *Cell Rep*. 2016;14(9):2041-9. doi:
911 10.1016/j.celrep.2016.02.011. PubMed PMID: 26923599; PMCID: PMC4785047.
- 912 46. Ishihara N, Fujita Y, Oka T, Mihara K. Regulation of mitochondrial morphology through
913 proteolytic cleavage of OPA1. *EMBO J*. 2006;25(13):2966-77. Epub 2006/06/17. doi:
914 10.1038/sj.emboj.7601184. PubMed PMID: 16778770; PMCID: PMC1500981.
- 915 47. Baker MJ, Tatsuta T, Langer T. Quality control of mitochondrial proteostasis. *Cold Spring
916 Harb Perspect Biol*. 2011;3(7). doi: 10.1101/cshperspect.a007559. PubMed PMID: 21628427;
917 PMCID: PMC3119916.
- 918 48. Zhang D, Zhang Y, Ma J, Niu T, W. C, X. P, Zhia Y, Sun F. Cryo-EM structures reveal
919 interactions of S-OPA1 with membrane and changes upon nucleotide binding. *bioRxiv*. 2019.
920 doi: <https://doi.org/10.1101/528042>.

- 921 49. Ge Y, Siegel AP, Jordan R, Naumann CA. Ligand binding alters dimerization and
922 sequestering of urokinase receptors in raft-mimicking lipid mixtures. *Biophys J.*
923 2014;107(9):2101-11. Epub 2014/11/25. doi: 10.1016/j.bpj.2014.09.021. PubMed PMID:
924 25418095; PMCID: PMC4223190.
- 925 50. Lewis RN, McElhaney RN. The physicochemical properties of cardiolipin bilayers and
926 cardiolipin-containing lipid membranes. *Biochim Biophys Acta.* 2009;1788(10):2069-79. Epub
927 2009/03/31. doi: 10.1016/j.bbamem.2009.03.014. PubMed PMID: 19328771.
- 928 51. Minner DE, Herring VL, Siegel AP, Kimble-Hill A, Johnson MA, Naumann CA. Iterative
929 layer-by-layer assembly of polymer-tethered multi-bilayers using maleimide-thiol coupling
930 chemistry. *Soft Matter.* 2013;9(40):9643-50. Epub 2013/10/28. doi: 10.1039/c3sm51446c.
931 PubMed PMID: 26029773.
- 932 52. Huang Y, Bharill S, Karandur D, Peterson SM, Marita M, Shi X, Kaliszewski MJ, Smith AW,
933 Isacoff EY, Kuriyan J. Molecular basis for multimerization in the activation of the epidermal
934 growth factor receptor. *eLife.* 2016;5. Epub 2016/03/29. doi: 10.7554/eLife.14107. PubMed
935 PMID: 27017828; PMCID: PMC4902571.
- 936 53. Comar WD, Schubert SM, Jastrzebska B, Palczewski K, Smith AW. Time-resolved
937 fluorescence spectroscopy measures clustering and mobility of a G protein-coupled receptor
938 opsin in live cell membranes. *J Am Chem Soc.* 2014;136(23):8342-9. doi: 10.1021/ja501948w.
939 PubMed PMID: 24831851; PMCID: PMC4063175.
- 940 54. Jaqaman K, Loerke D, Mettlen M, Kuwata H, Grinstein S, Schmid SL, Danuser G. Robust
941 single-particle tracking in live-cell time-lapse sequences. *Nat Methods.* 2008;5(8):695-702. Epub
942 2008/07/22. doi: 10.1038/nmeth.1237. PubMed PMID: 18641657; PMCID: PMC2747604.
943

Figure 1

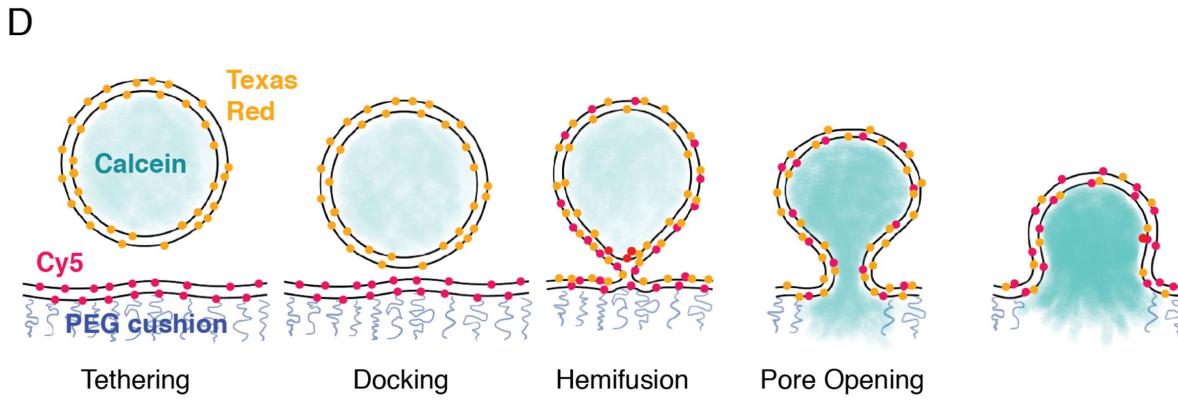
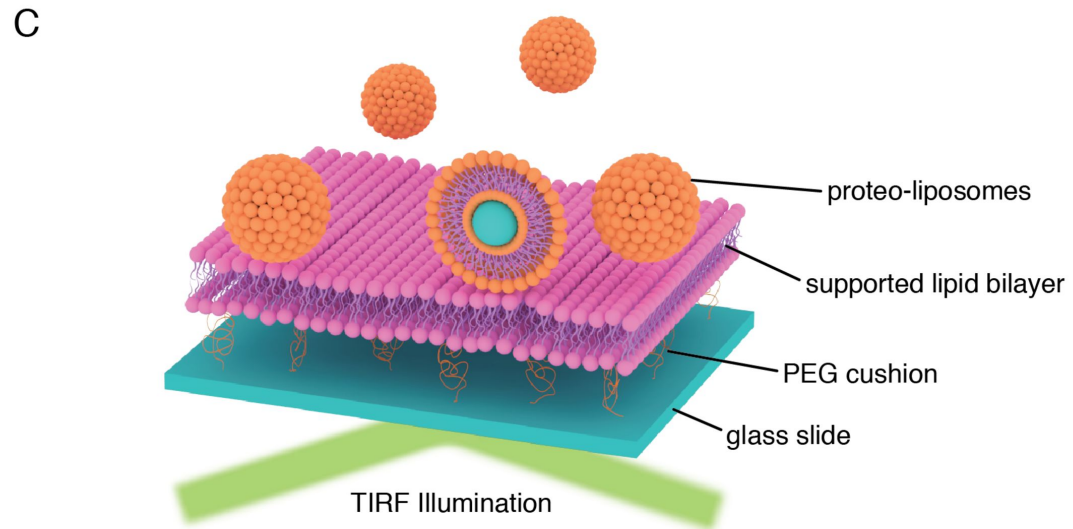
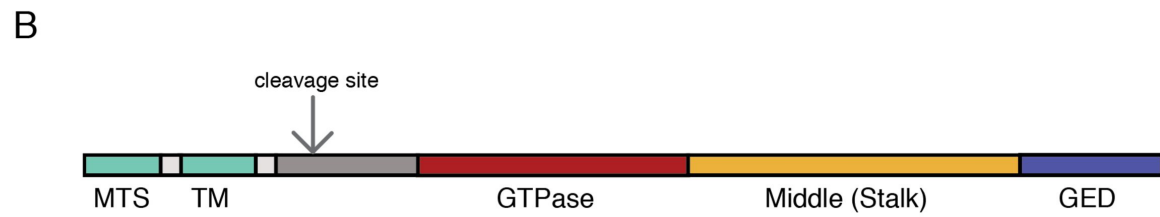
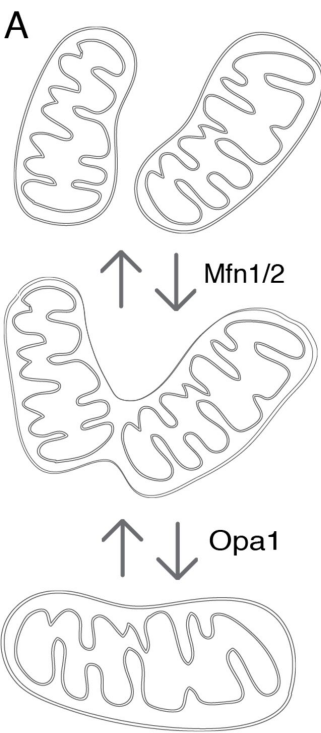


Figure 2

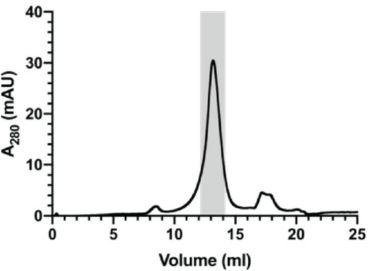
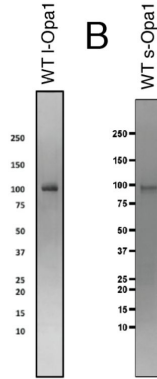
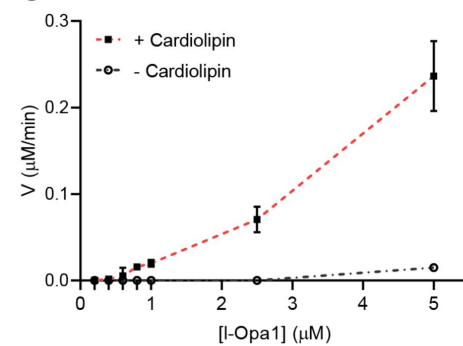
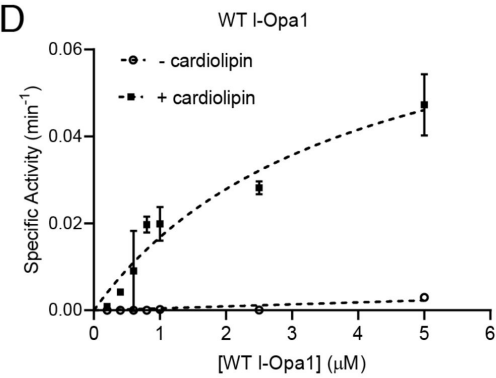
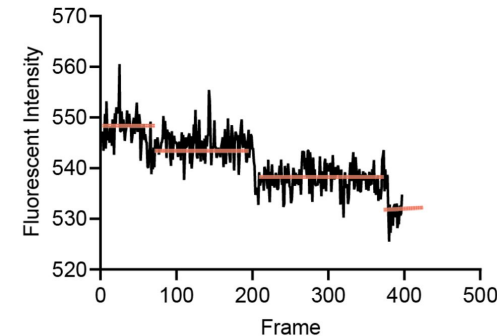
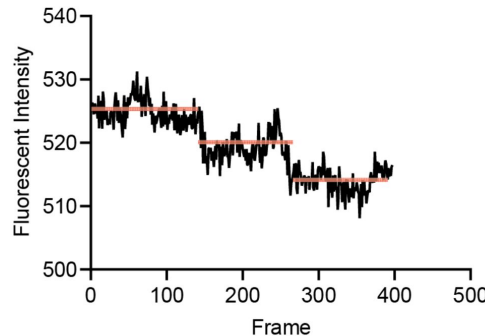
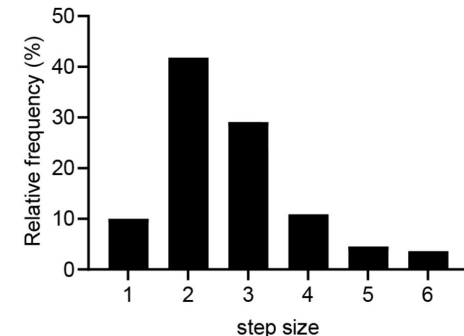
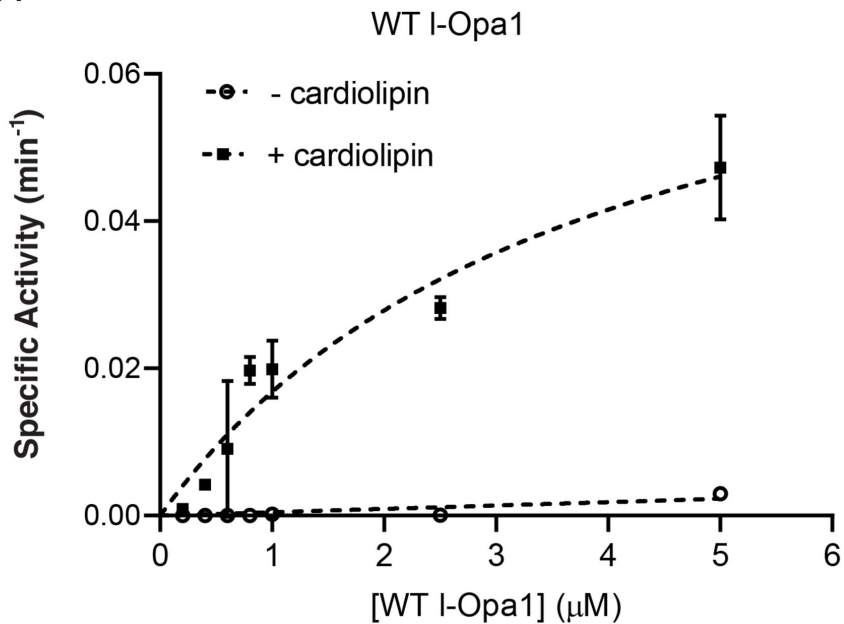
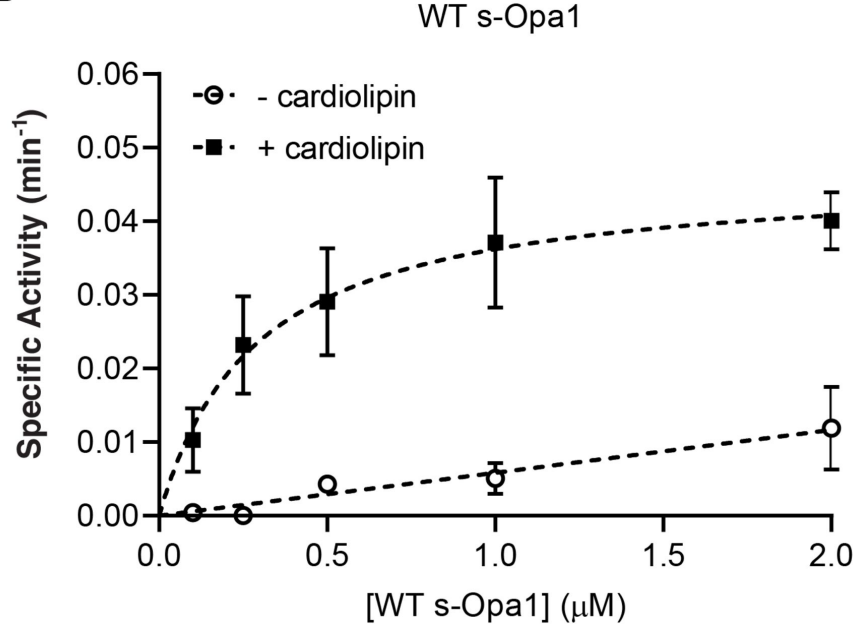
A**B****C****D****E****F****G**

Figure 2-figure supplement 1

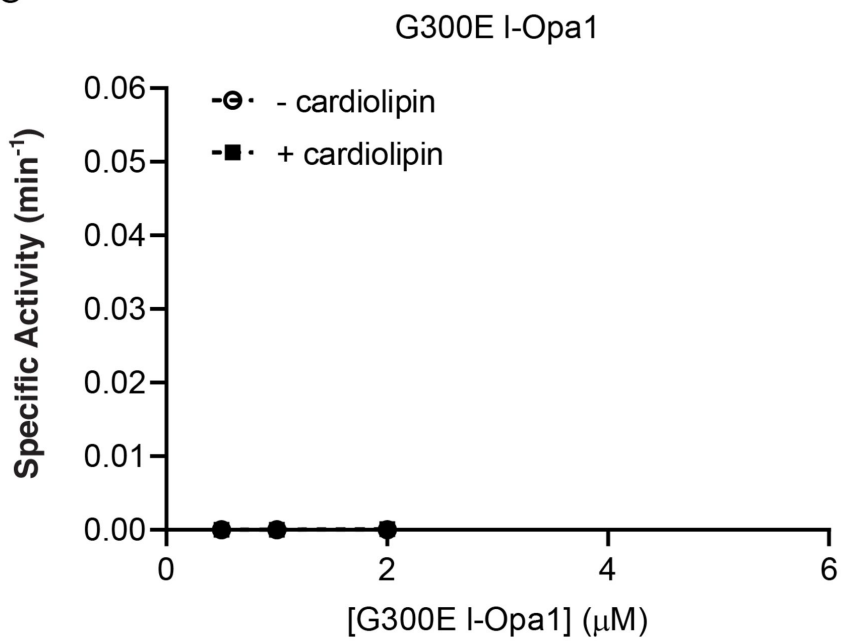
A



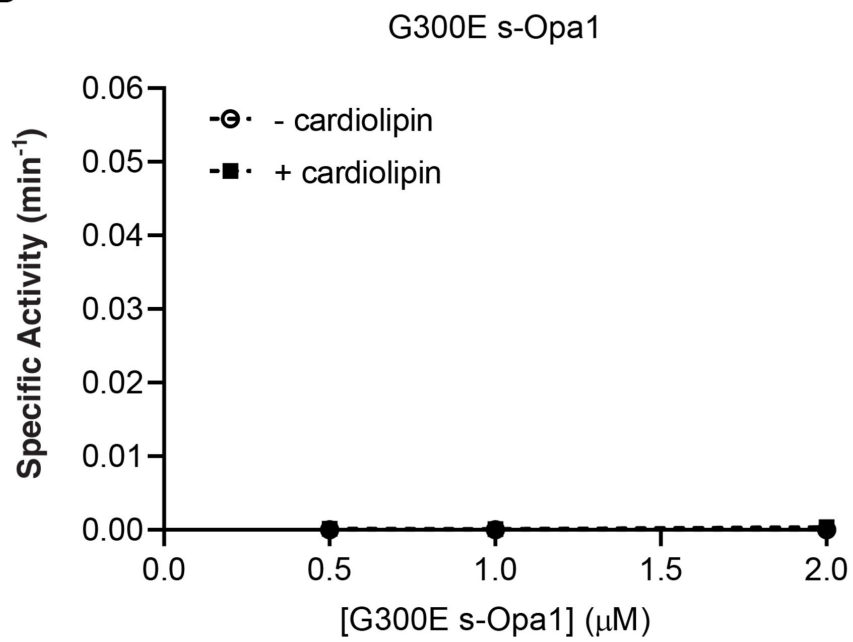
B



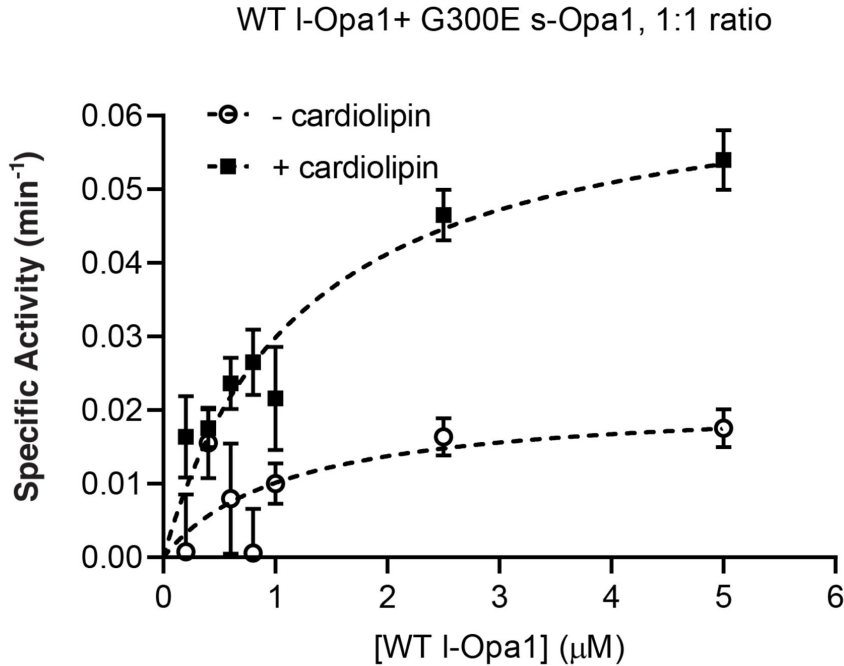
C



D



E



F

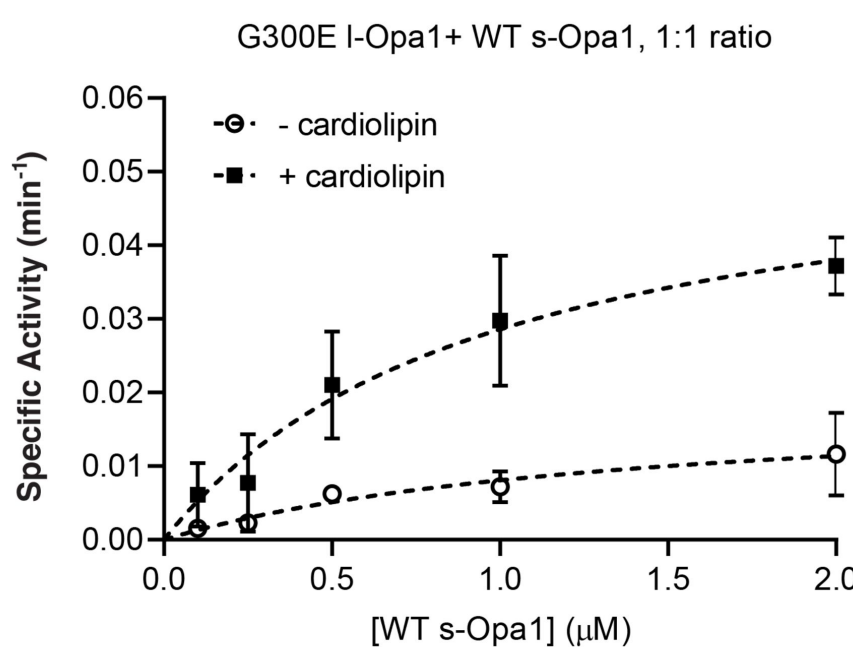
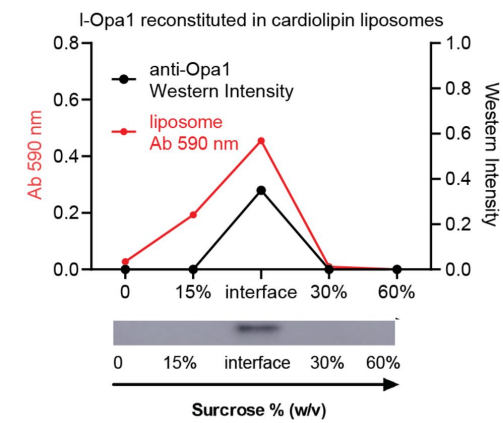
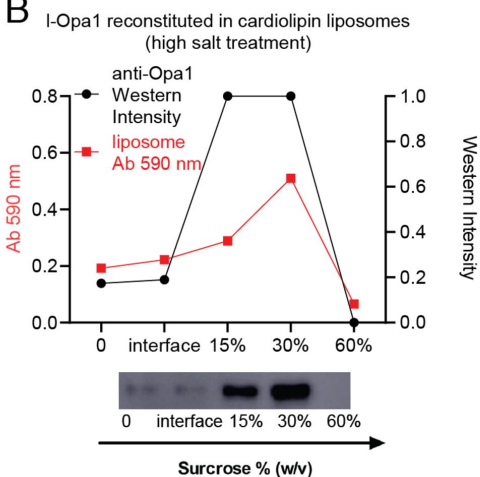


Figure 2-figure supplement 2

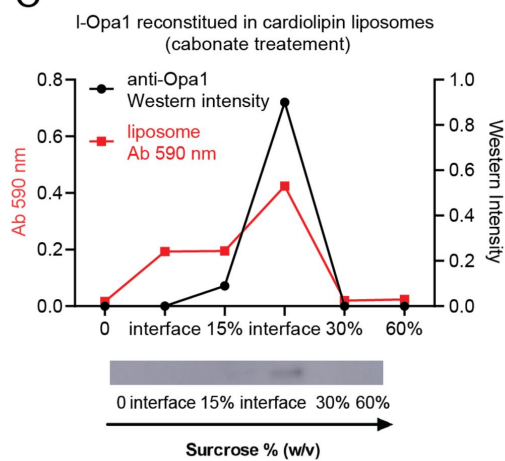
A



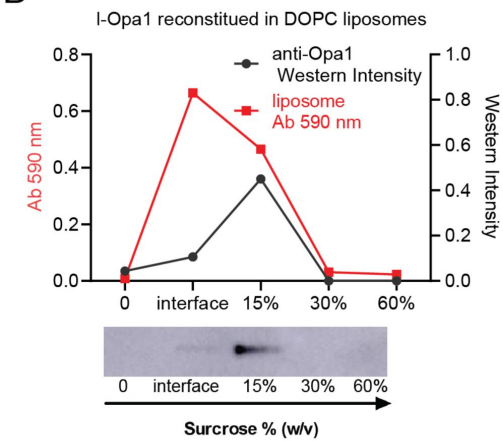
B



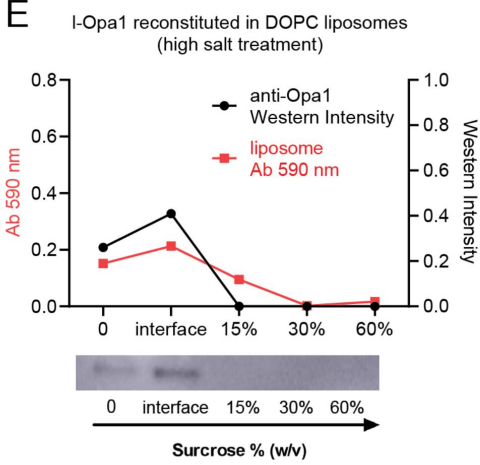
C



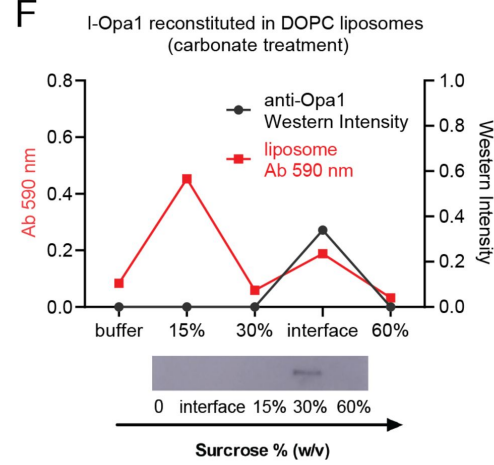
D



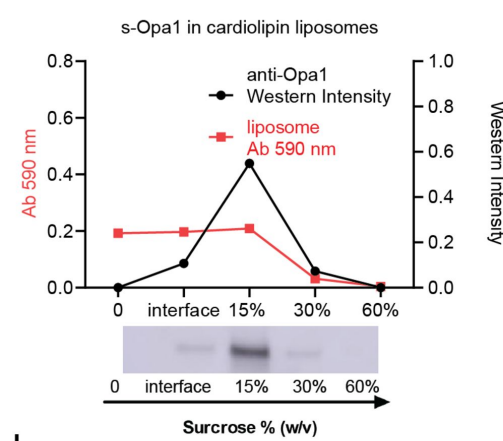
E



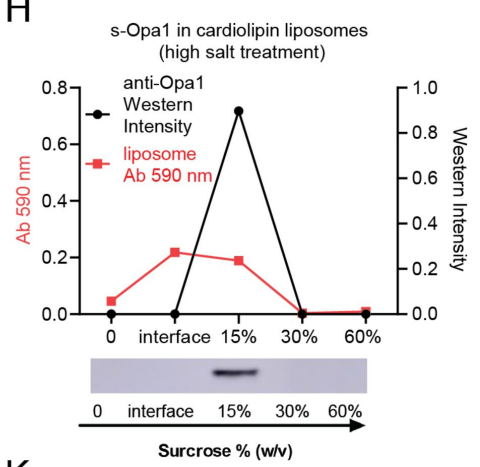
F



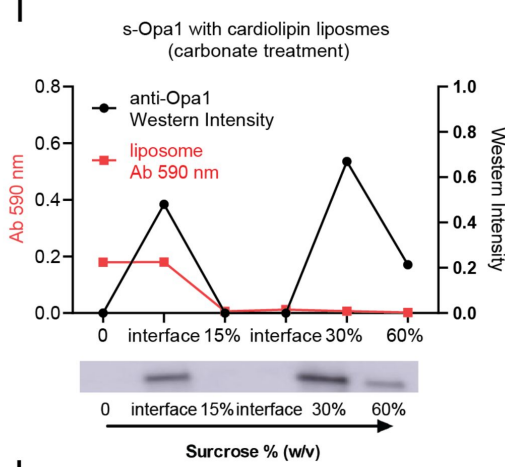
G



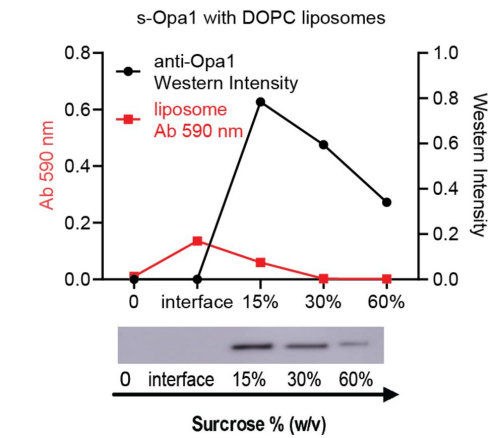
H



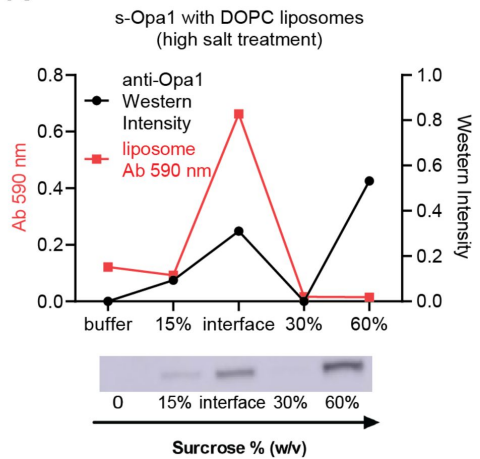
I



J



K



L

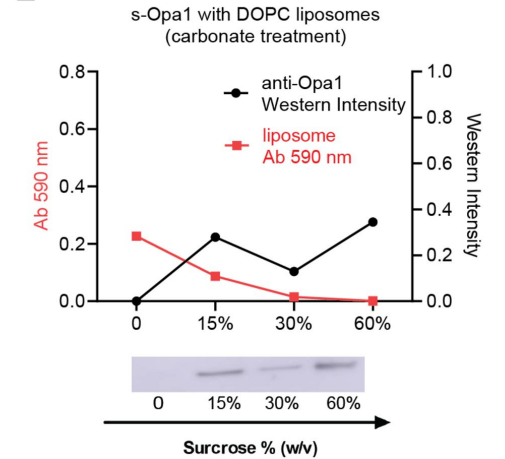


Figure 2-figure supplement 3

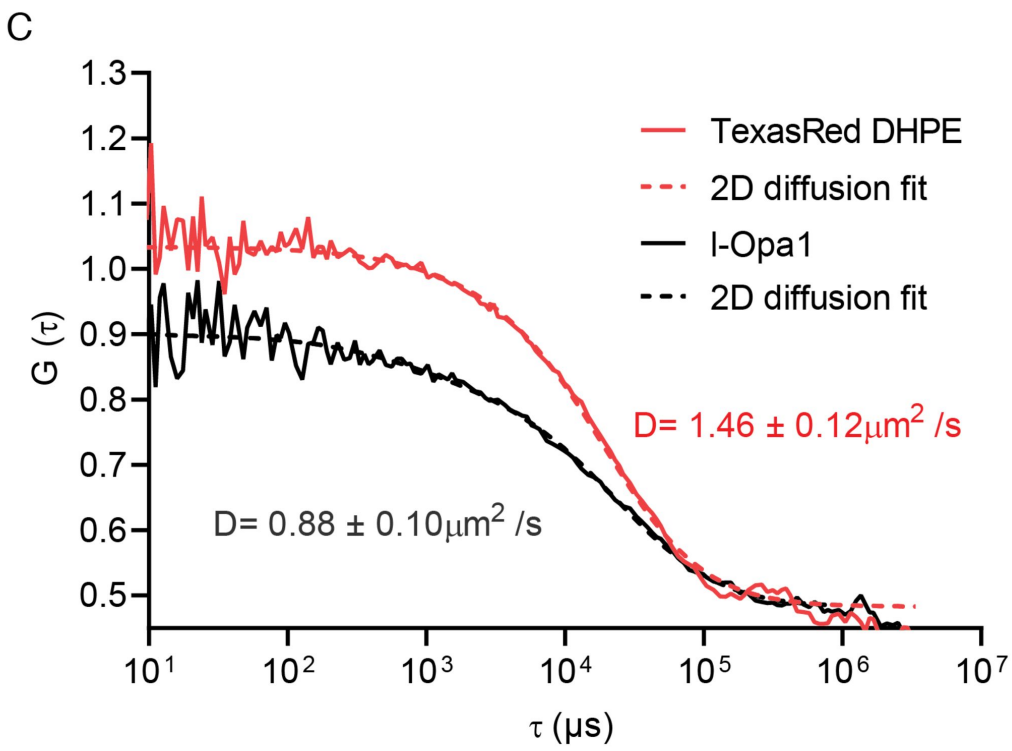
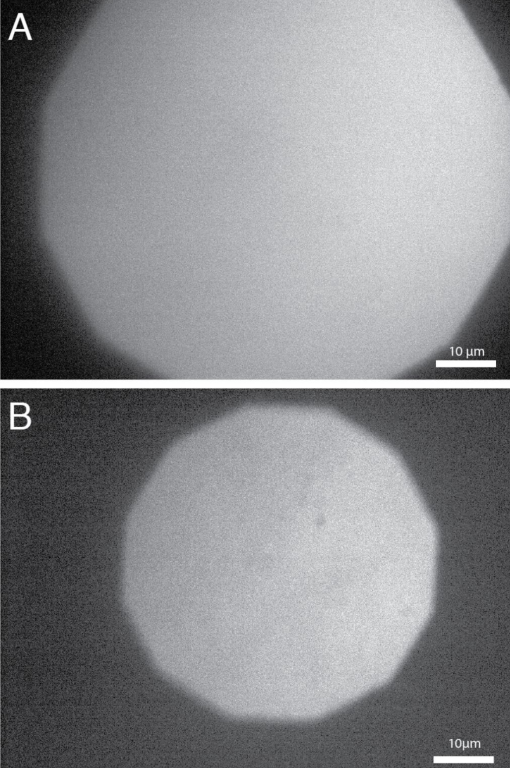
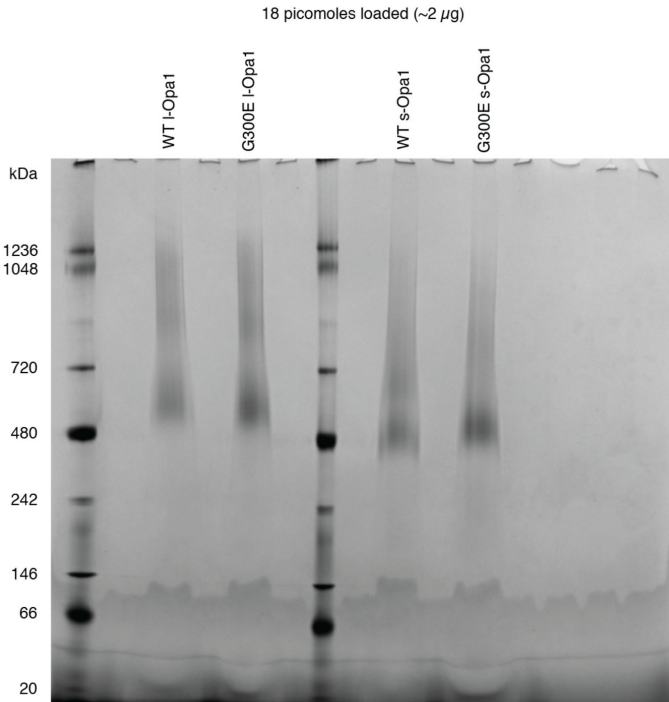


Figure 2-figure supplement 4

A



B

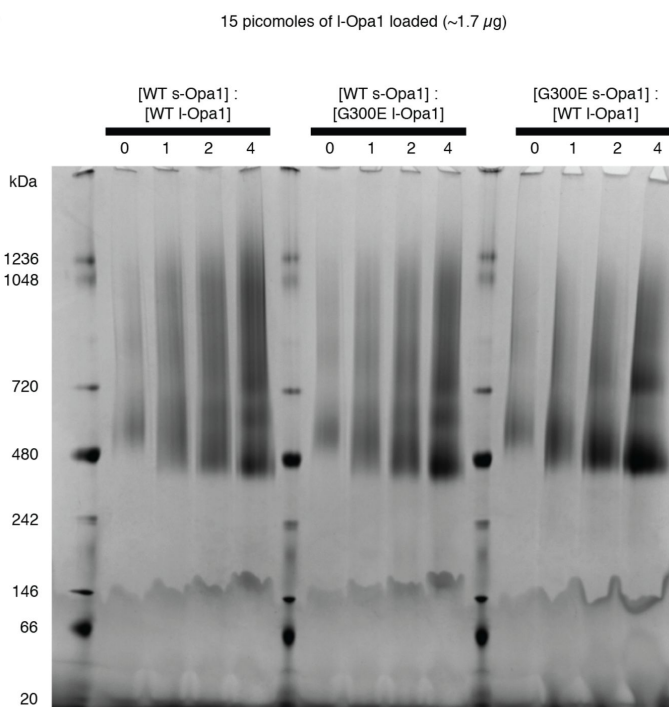
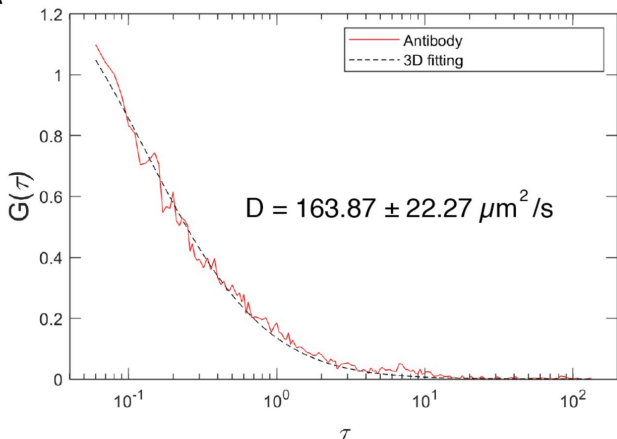
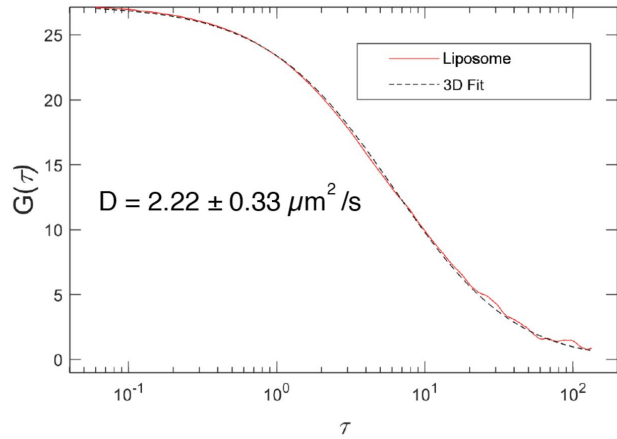


Figure 2--figure supplement 5

A



B



C

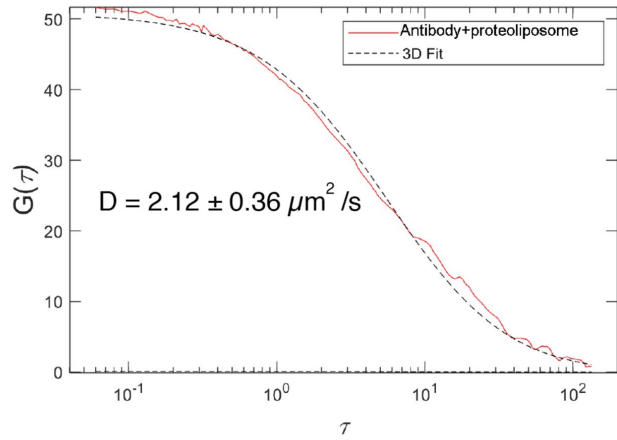
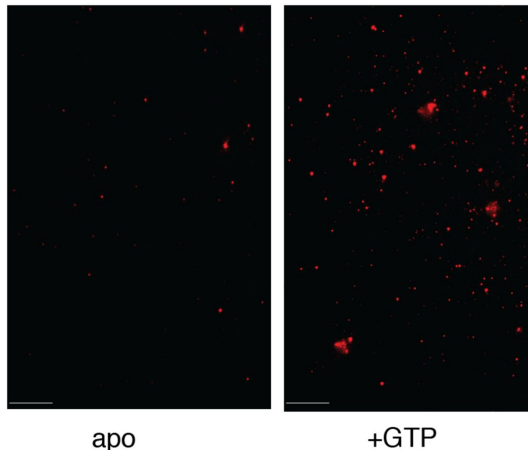
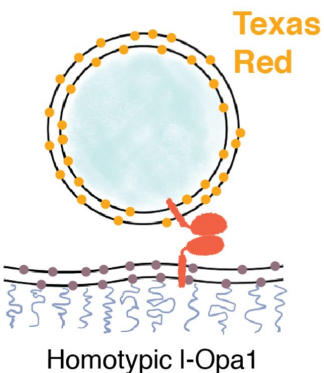
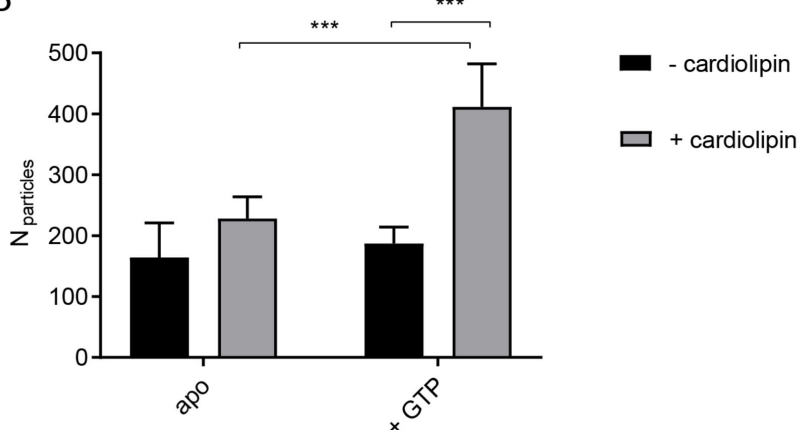


Figure 3

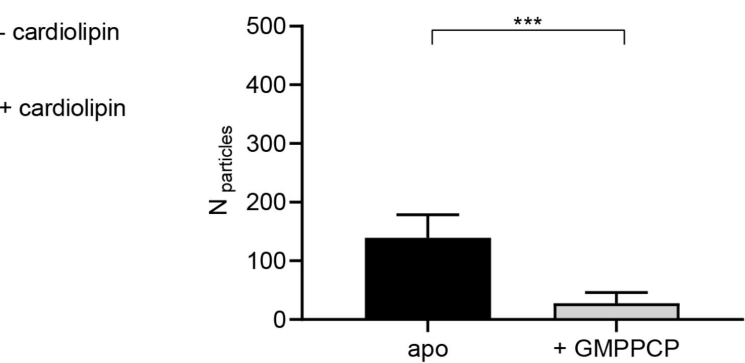
A



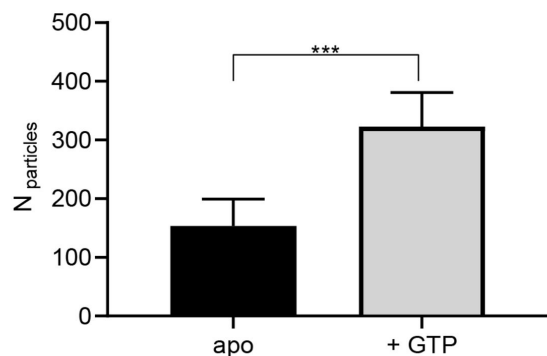
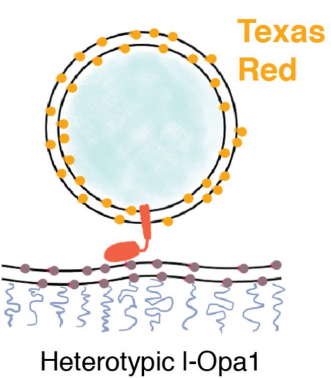
B



C



D



E

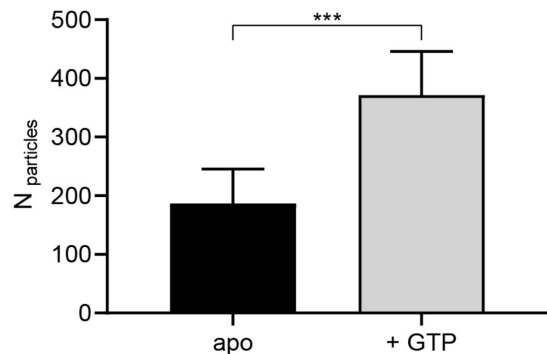
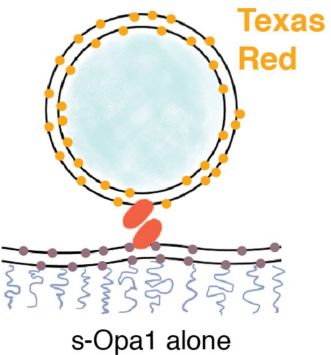
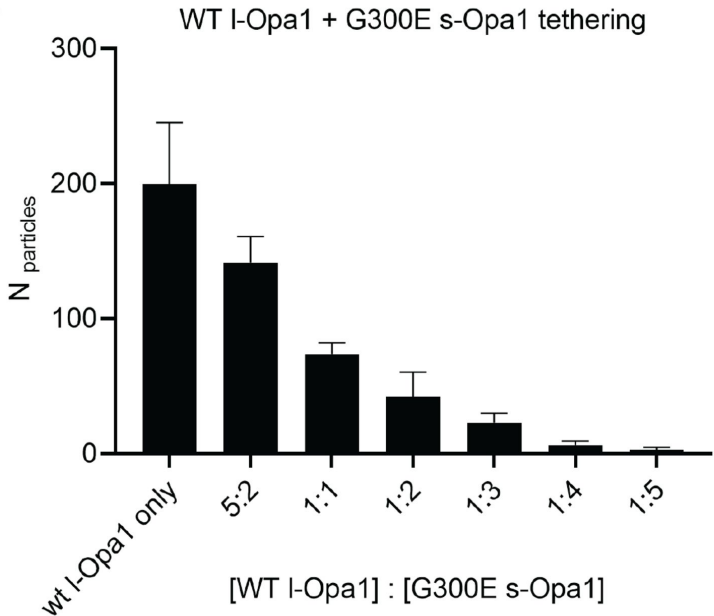


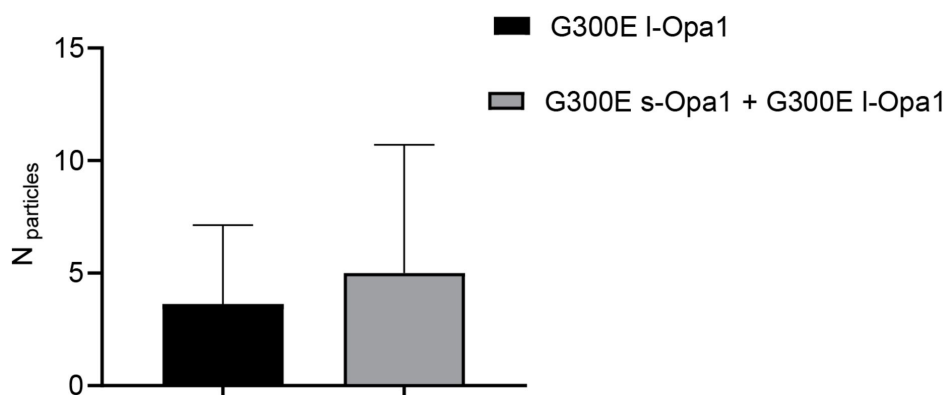
Figure 3-figure supplement 1

A



B

G300E I-Opa1 and
G300E I-Opa1 + G300E s-Opa1
liposome tethering



C

G300E I-Opa1 + WT s-Opa1 tethering

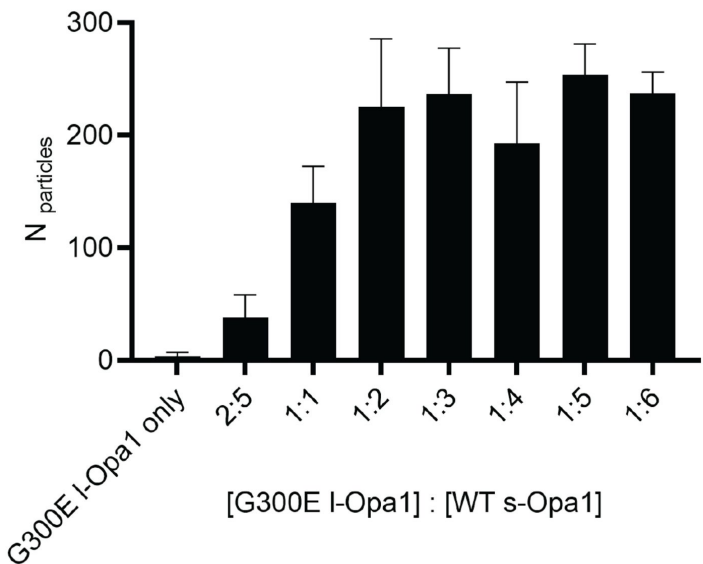


Figure 3-figure supplement 2

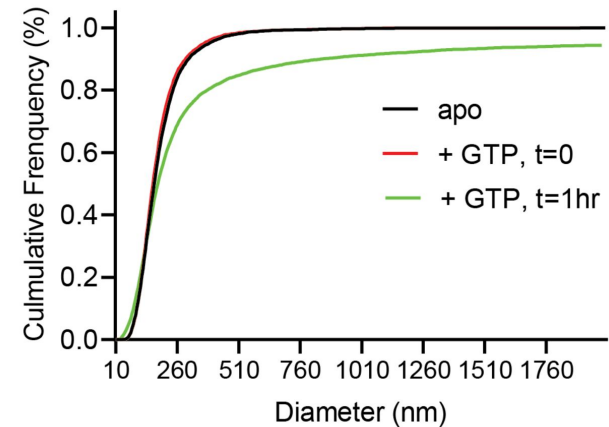
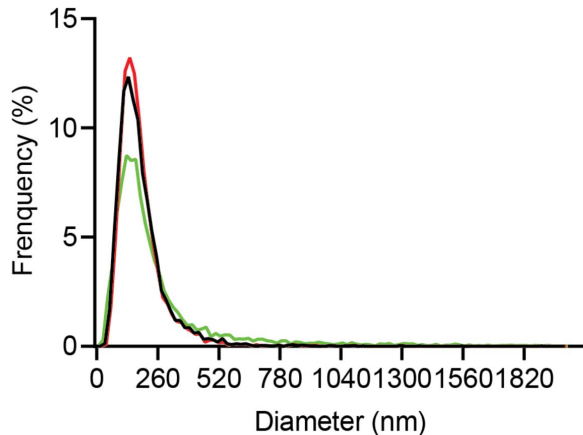
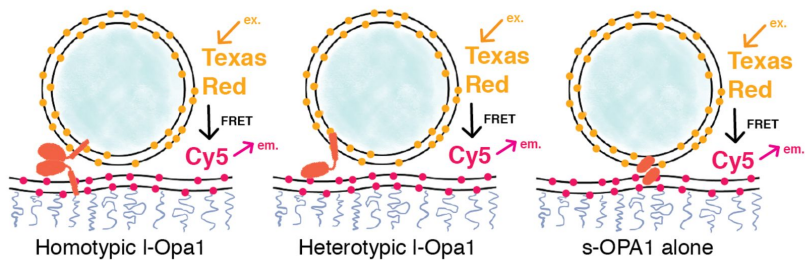
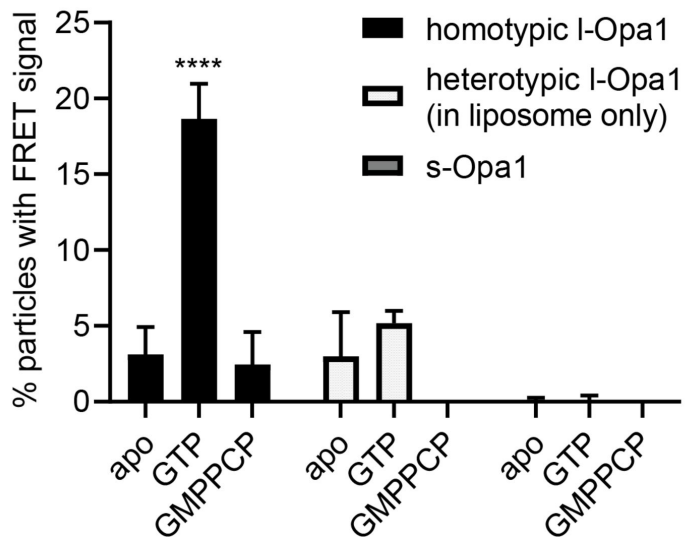
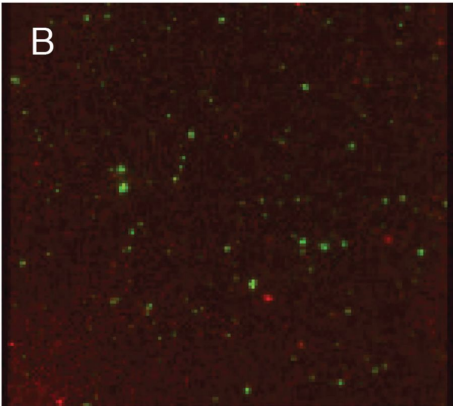


Figure 4

A



B



C

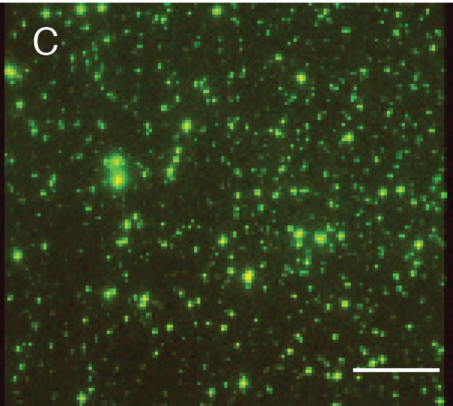
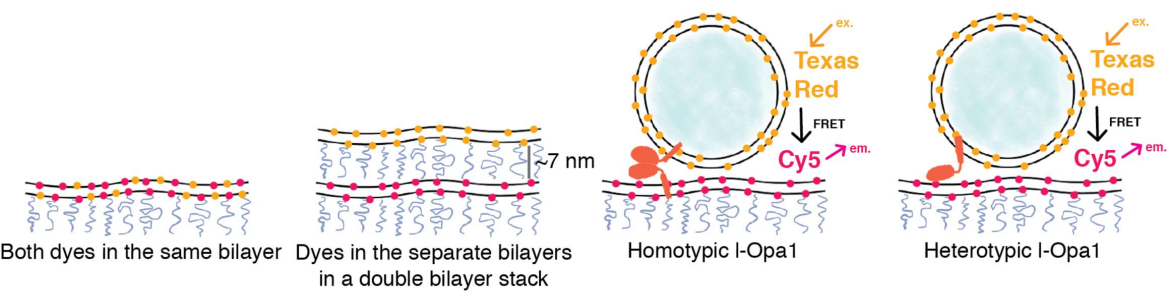
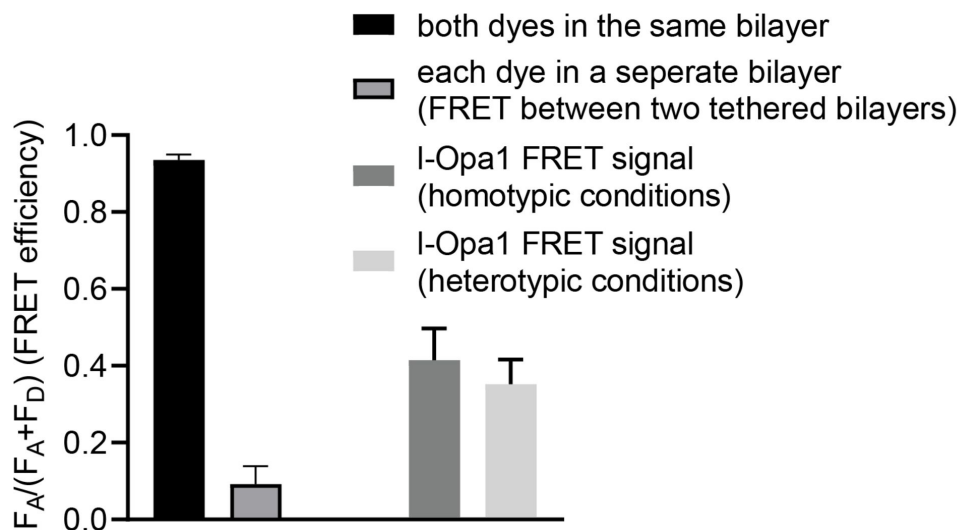


Figure 4-figure supplement 1

A



B

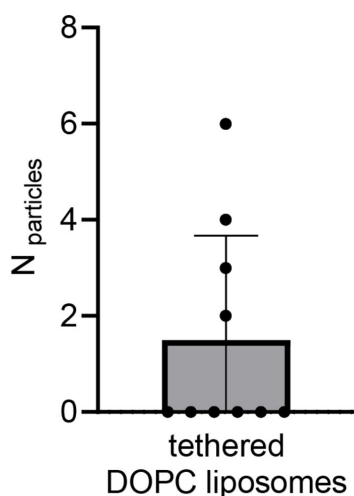


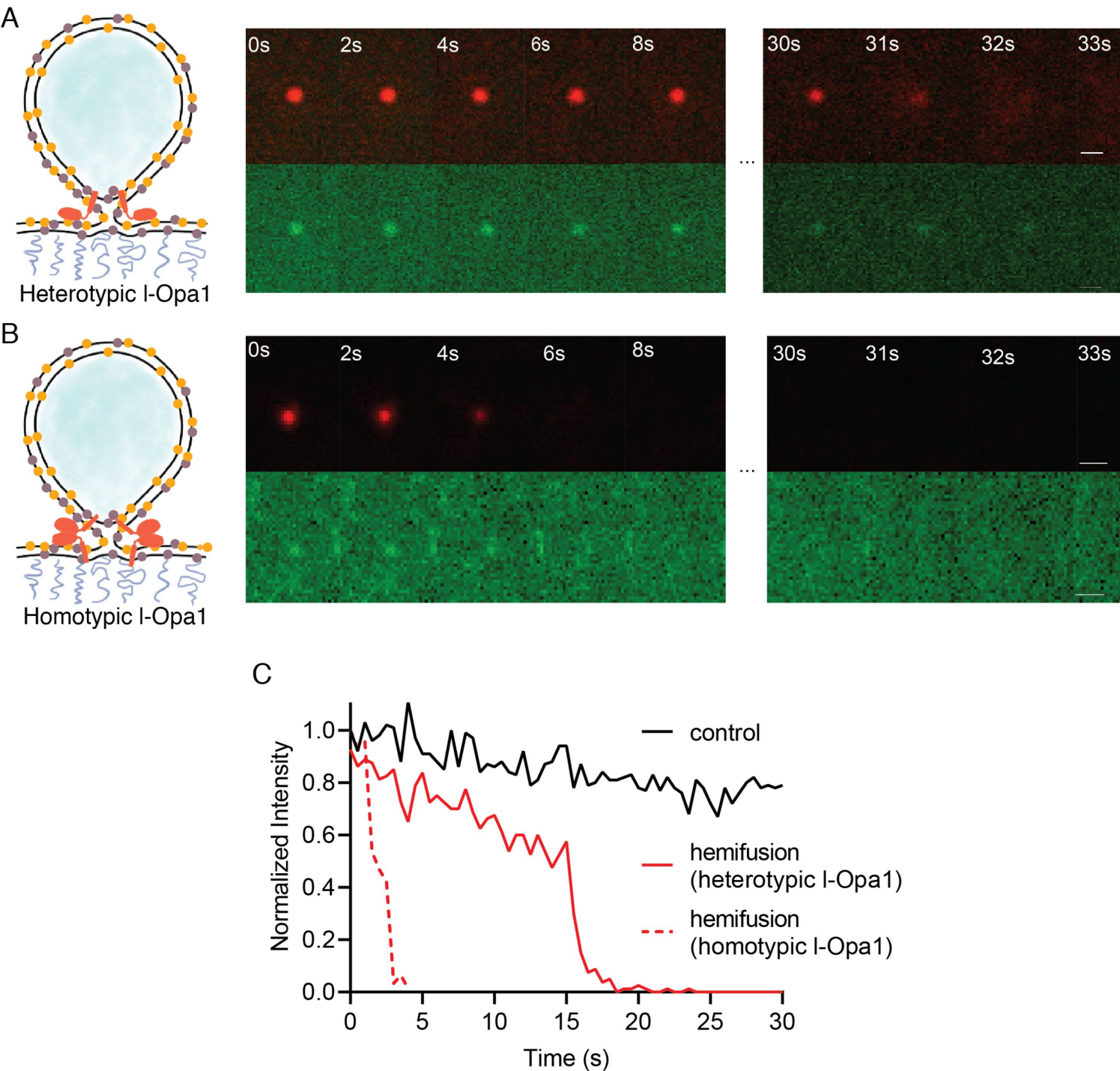
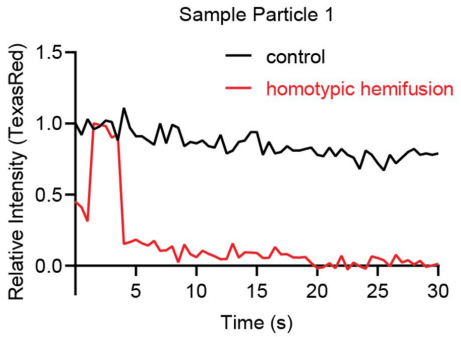
Figure 5

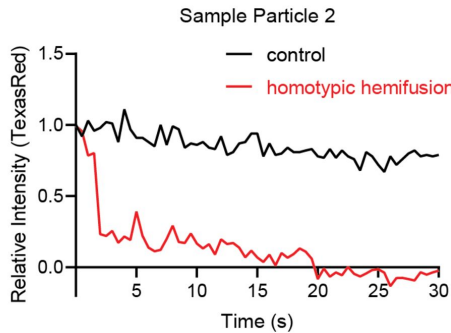
Figure 5-figure supplement 1

A. Additional examples of homotypic hemifusion:

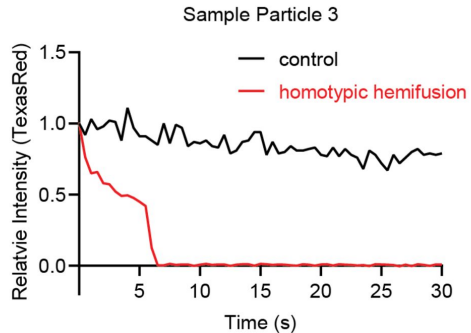
i.



ii.

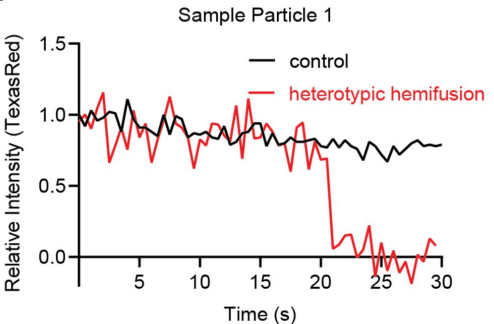


iii.

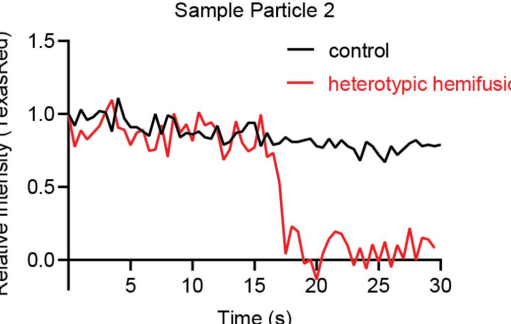


B. Additional examples of heterotypic hemifusion

i.



ii.



iii.

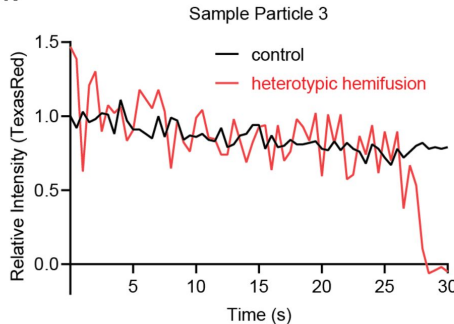
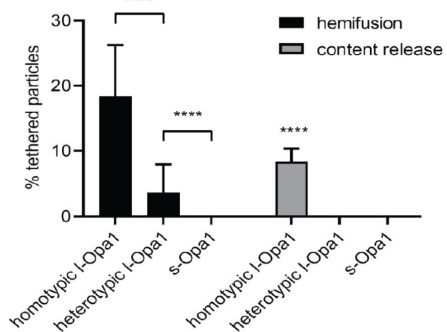
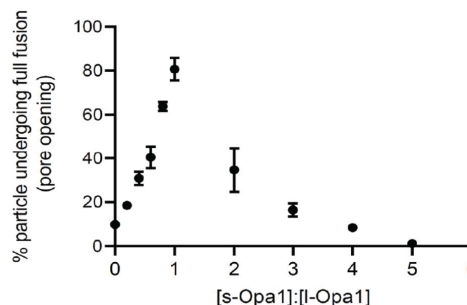


Figure 6

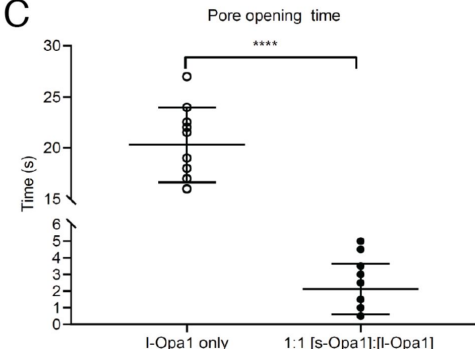
A



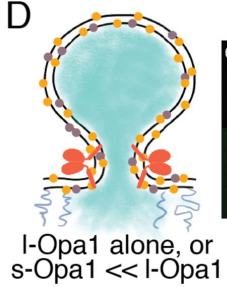
B



C

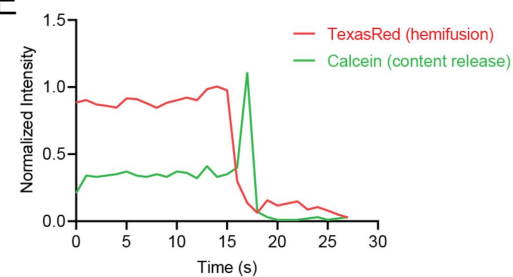


D

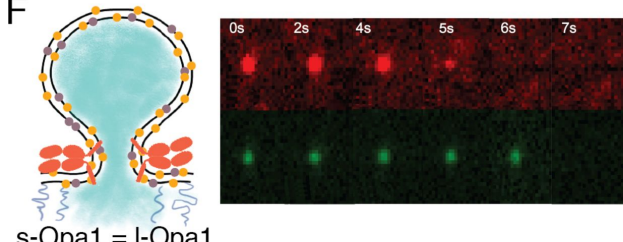


I-Opa1 alone, or
s-Opa1 << I-Opa1

E



F



s-Opa1 = I-Opa1

G

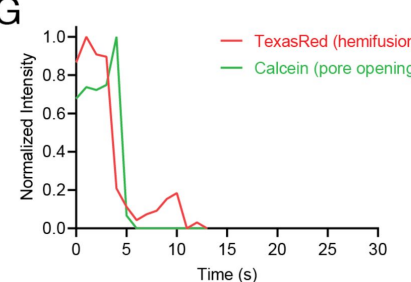
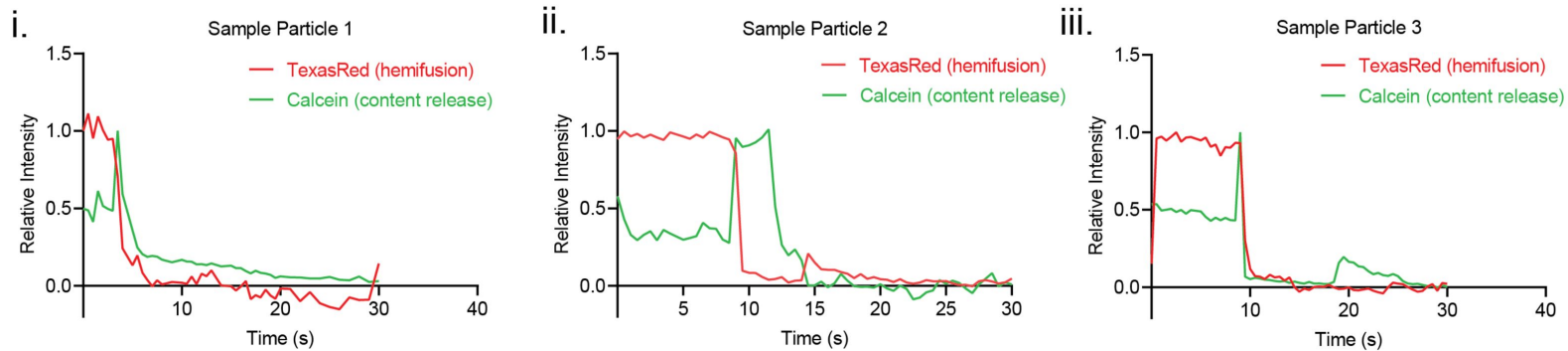


Figure 6-figure supplement 1

A. Additional examples of I-Opa1 (on both bilayers) hemifusion and pore opening



B. Additional examples of I-Opa1 (on both bilayers) + s-Opa1 hemifusion and pore opening

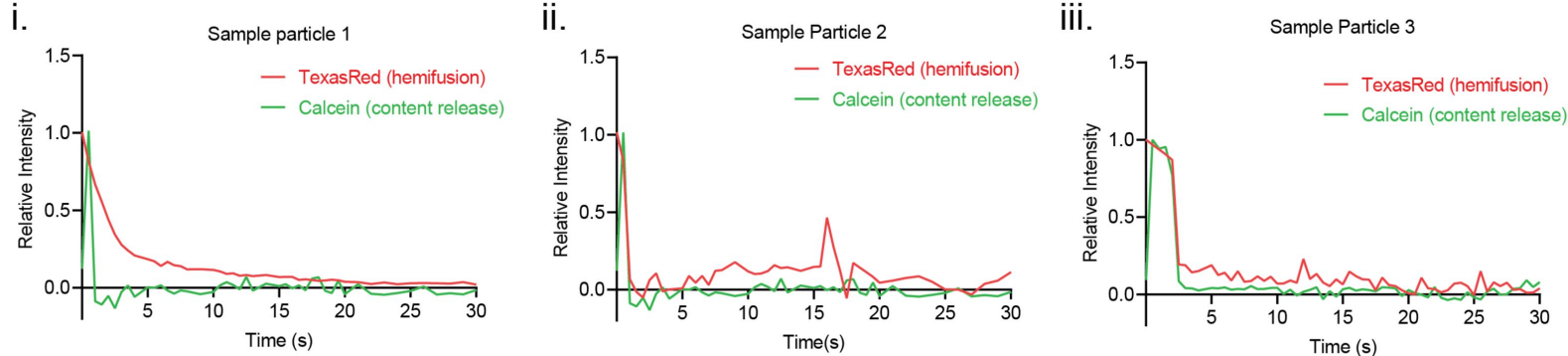


Figure 7

